LUNFD6/(NFFL-7210)2002

A study of diffractive scattering in electron-proton collisions at HERA

Diploma Thesis
by

Albert Knutsson

LUND
UNIVERSITY

DEPARTMENT OF ELEMENTARY PARTICLE PHYSICS
LUND, 2002

Contents

Chapter 1

Introduction

1.1 Introduction to Particle Physics

The concept of particle physics is to study the fundamental constituents of matter and their interactions. The present theory to describe the fundamental interactions is called the *standard model*. It divides the interactions of nature into four forces; gravity, electromagnetism and the weak and strong forces. Gravity can at a microscopic level be neglected and we therefore only have to deal with three forces. This is valid up to energies of present accelerators, for higher energies the standard model predicts a unification of all three forces. In the standard model matter and forces in the universe are described by three kinds of particles, the leptons, the quarks and the gauge bosons. All three kinds of particles are assumed to be elementary, i.e. they are point-like and are assumed to have no internal structure. This also involves that they can not be excited.

The leptons and the quarks are fermions and are thus spin-$\frac{1}{2}$ particles. These are basically the building blocks of nature. The gauge bosons are spin-1 particles and these are the force mediators, acting as forces between leptons, between quarks or between quarks and leptons, and in some cases also between bosons. Each force has its own force carriers. Particles interacting through a force are exchanging the gauge bosons of the certain force. The exchange bosons are created by "borrowing" energy from the vacuum according to Heisenbergs uncertainty principle

$$\Delta t \cdot \Delta E \sim \hbar \tag{1.1}$$

where ΔE is the energy used within the time Δt. Using $E \sim mass$ and approximating the distance travelled by a particle by $\Delta t \cdot c$, a force interacting through a heavier gauge boson thus has a shorter spatial range compared to one interacting through a lighter gauge boson.

The interacting particle of the electromagnetic force is the photon, γ. It can only couple to particles carrying electromagnetic charge. The photon can not couple to itself. Since the photon is massless the range of the electromagnetic force is infinite. The electromagnetic

force keeps the electrons in the cloud around the atomic nuclei, and keeps also the atoms together in a crystal.

The interacting bosons of the weak force are the Z^0, W^+ and W^- particles. These particles are massive, compared to the photons and the weak interaction has thus a limited range. It is the weak interaction that is responsible for different decays e.g. β-deacys. Whenever an exchange of a photon is possible, also an exchange of a Z^0 is possible. The electromagnetic and the weak force are unified through an electroweak theory.

The charge of the strong force is called colour. It is the strong force that binds the quarks together inside non-elementary particles like hadrons and mesons, and also binds the nucleons together inside the nuclei. The hadrons consist of three quarks whereas the mesons are constructed from a quark and an anti-quark. Historically the color charge had to be introduced to avoid the Pauli principle to be violated. For example the Δ^{++}-baryon is a hadron built up of three identical quarks with exactly the same quantum numbers if the colour is not considered. The interacting particles of the strong force are the gluons. Since the gluons carry colour charges themselves they can couple to themselves. One is talking about the selfcoupling of the gluon. As we will see in the thesis this selfcoupling leads to a higher complexity in reactions involving the strong force. Due to the selfcoupling of the gluons the field force will be resticted to a narrow field tube between the colour charges, having a constant energy density. The gluons come in different colour states. The 6 different colours; blue, green, red, and the anticolours; anti-blue, anti-green and anti-red, can be combined into 8 different colour singlet states.

There are 6 different leptons, divided into three different generations. The common known electron belongs to the first generation.

$$\begin{pmatrix} e^- \\ \nu_e \end{pmatrix} \begin{pmatrix} \mu^- \\ \nu_\mu \end{pmatrix} \begin{pmatrix} \tau^- \\ \nu_\tau \end{pmatrix}$$

The electron, the muon and the tauon all have the electromagnetic charge -1, and thus interact electromagnetically, while the neutrinos (ν) are neutral and do not. All leptons interact weakly.

The quarks are strongly interacting particles, carrying color charge, but they are also interacting electromagnetically and weakly. There are six different quarks, also called flavours, which like the leptons are divided into three generations. The six flavours have exotic names as up(u), down(d), charm(c), strange(s), top(t) and bottom(b).

$$\begin{pmatrix} u \\ d \end{pmatrix} \begin{pmatrix} c \\ s \end{pmatrix} \begin{pmatrix} t \\ b \end{pmatrix}$$

The up-type quarks (u, c, t) in each generation carry the electromagnetic charge $+\frac{2}{3}$, whereas the down-type quarks (d, s, b) carry the electromagnetic charge $-\frac{1}{3}$. Each quark, except the lightest one, can due to the weak force decay into the next lighter quark. Thus the explanation of the β-decay of the neutron is given by the $uud \longrightarrow udd + e^+ + \nu_e$ reaction, where an u-quark in the neutron decays in to a d-quark, a positron (i.e. an anti-electron) and a neutrino.

Each elementary particle in the standard model has an antiparticle with opposite properties, e.g. charge, but the same mass as the particle. Theoretically the concept of antiparticles is a consequence of the unification of special relativity and quantum mechanics, first performed by P.A. Dirac who derived the relativistic Schrödinger equation in 1928.

To investigate the properties of the elementary particles by creating physical states that do not exist in "our daily life" one needs high energies, and this is why large collider facilities like those in DESY, CERN, Fermilab, Brookhaven and others have been built. A detailed investigation of the structure of hadrons requires high energies, and experiments at DESY study the structure of the proton by colliding electrons and protons at high energies. Accelerators and their detectors are large microscopes helping us look into what in common language is known as microcosmos. The accelerator can be compared to a light-source and the detector as a microscope. The large kinetic energy of the accelerated particle is used to induce physical reactions, such that part of the kinetic energy in the end turns into particles that can be measured in our detectors.

1.2 Thesis Introduction

The thesis starts with a general presentation of high energy physics detectors used in the H1 detector at DESY (chapter 2) from which the data used in this analysis is collected. A chapter dealing with the basic theory that has to be understood for the thesis then follows (chapter 3). This chapter can be divided into two parts, one is treating the general deep inelastic scattering[1] and the parton[2] dynamics, the other part is treating the diffractive deep inelastic scattering[3]. The next chapter describes how events[4] interesting for this analysis were selected from the data, where the event selections made on the data are described (chapter 4). The different requirements on the kinematic variables are explained. We also take a look at the event display, which is a good way of visualizing events (chapter 5). After this follows a short introductory study of forward jets[5] in deep in elastic scattering (chapter 7). The next chapter contains a Monte Carlo study of the relevance of different exchange mechanisms used to describe diffractive deep inelastic scattering (chapter 8). In chapter 9 the ratio of diffractive deep inelastic scattering forward jet events to all deep inelastic scattering forward jet events is studied. In this chapter the result of the analyses is presented. The thesis ends with a chapter on the possibility to determine the asymmetry in the angular distribution of the scattering plane of the electron with respect to the scattering plane of the proton in diffractive deep inelastic scattering using a the very forward proton spectrometer, planned to be build in the future as a complementary proton detector (chapter 10). The footnotes in this introduction are just short explanations that will be explained in more detail in the thesis, especially in the theory chapter.

[1] The most commonly occurring reaction at high energy electron-proton collisions.

[2] The building blocks of the proton.

[3] A special kind of deep inelastic scattering where the proton not is fragmented into partons when it is struck by electron. The signature of such a reaction is that no energy is detected in a specific region of the detector.

[4] Every recorded electron-proton collision is referred to as an event.

[5] A jet is a collimated flow of particles commonly occurring in high energy particle collisions.

Chapter 2

DESY and HERA

DESY, which stands for Deutsches-Electronen-Synchrotron, is located in Hamburg, Germany, and is one of the leading high energy physics laboratories in the world. The present research in particle physics is centered around the main-accelerator, HERA. HERA, with a circumference of 6.3 km, is the only circular electron-proton collider in the world. Before the electrons are injected into the HERA-ring they are accelerated in several pre-accelerators starting with the LINAC (from 0 to 450 MeV), the DESY-II (to 7 GeV) and the PETRA-II rings (to 13 GeV). The protons, which are injected into HERA from the opposite direction compared to the electrons, are accelerated in the LINAC-II (from 0 to 50 MeV), the DESY-III (to 7.5 GeV) and the PETRA-II rings (to 40 GeV). After the final acceleration in HERA, the electrons have an energy of 27.5 GeV and the protons an energy of 920 GeV. The energy of the electrons is limited, to around 30 GeV, by their energy loss through synchrotron radiation. The collisions of the two particle beams result in a total center of mass energy $\sqrt{s} \approx 300$ GeV.

Most of the time positrons, for which it is easier to obtain a high current, are accelerated instead of electrons. It has turned out that the electrons are absorbed by positive ions generated by the vacuum pumps, disturbing the negative current. From now on "electron" stands for the accelerated lepton in general. The protons and the electrons are accelerated in bunches, and the bending of the protons in the HERA-ring are performed by 4.7 T superconducting magnets, cooled by liquid helium, whereas the bending of the electrons, due to their lower energy, only need normal conducting magnets.

2.1 The H1 detector at HERA

The various detector components provide information about the different variables describing an event. To select a specific event class, cuts are made in these kinematic variables on detector level, and a good understanding of the data therefore requires that the performance of the detector components are accurately known.

The general description of different detector components in section 2.2 is based on information given in [1]. For the description of the H1-detector in section 2.3-2.5 I have

used [2, 3, 4, 5]. However a general description of the detector can be found in most theses written within the H1 Collaboration.

The H1 detector is one of the four main detectors positioned at the four interaction points of the HERA collider. It is a complex system consisting of many subdetectors. The first version of the H1 detector was completed in 1991. Since then it has been upgraded at several occasions. Its weight is about 2800 tons and it measures $12 \times 10 \times 15$ m^3.

The coordinate system of H1 is defined such that the z-axis is along the proton direction, the y-axiz is vertical and the x-axis is pointing towards the center of the HERA ring. Thus, the polar angle $\theta = 0^o$ is the proton forward direction, and $\theta = 180^o$ is identical to the incoming electron direction. The azimuthal angle is denoted by ϕ.

Describing the full detector and the way data are treated in detail, is too big a task for a master thesis. I therefore only deal with its main components and the parts related to this thesis. As can be seen in fig. 2.1 the detector is symmetric in $r - \phi$, while it is asymmetric along the beam direction (the z-direction). This is because of the different beam energies of the electrons and the protons. Since the protons have a much higher energy, the center of mass system will be boosted into the proton direction (called the forward direction). Therefore the detector has a much more massive construction in the forward direction, and has to have higher resolution in the region closest to the forward proton direction.

The three main parts of the H1 detector, or for high energy physics detectors in general, are the tracking device, the calorimeters and the muon system. Much effort has been invested into the precision of the measurement of the electron. If one knows the kinematics of the electron before and after scattering one also knows the kinematics of the photon exchanged in the collision. It is the photon that probes the proton and induces the reactions studied at H1.

In general a high energy detector is constructed as follows. The whole detector is built up around the collision vertex. Closest to the collision vertex is the tracking system. It is positioned inside a magnetic field, which makes it possible to measure the momentum of the charged particles. The calorimetric system surrounds the tracking detectors, and finally the calorimeter is surrounded by the muon system. The detector is shielded by concrete blocks that protects the environment outside the detector from radiation created on the inside.

2.2 Detectors in Particle Physics

Several different principles are used to detect particles. Measurement of ionization created by charged particles and energy deposition in totally absorbing detectors are commonly used methods. Radiative methods such that detection of Cherenkov radiation and transition radiators are used to identify particles. Cherenkov counters are not used in H1. Muons do not interact very strongly with matter, and can thus traverse all the material of the detector. This is used as a typical signature of muons. Furthermore, for the determination of the momentum of charged particles one uses that it is proportional to the bending radius perpendicular to the field lines in the magnetic field and to the magnetic field strength.

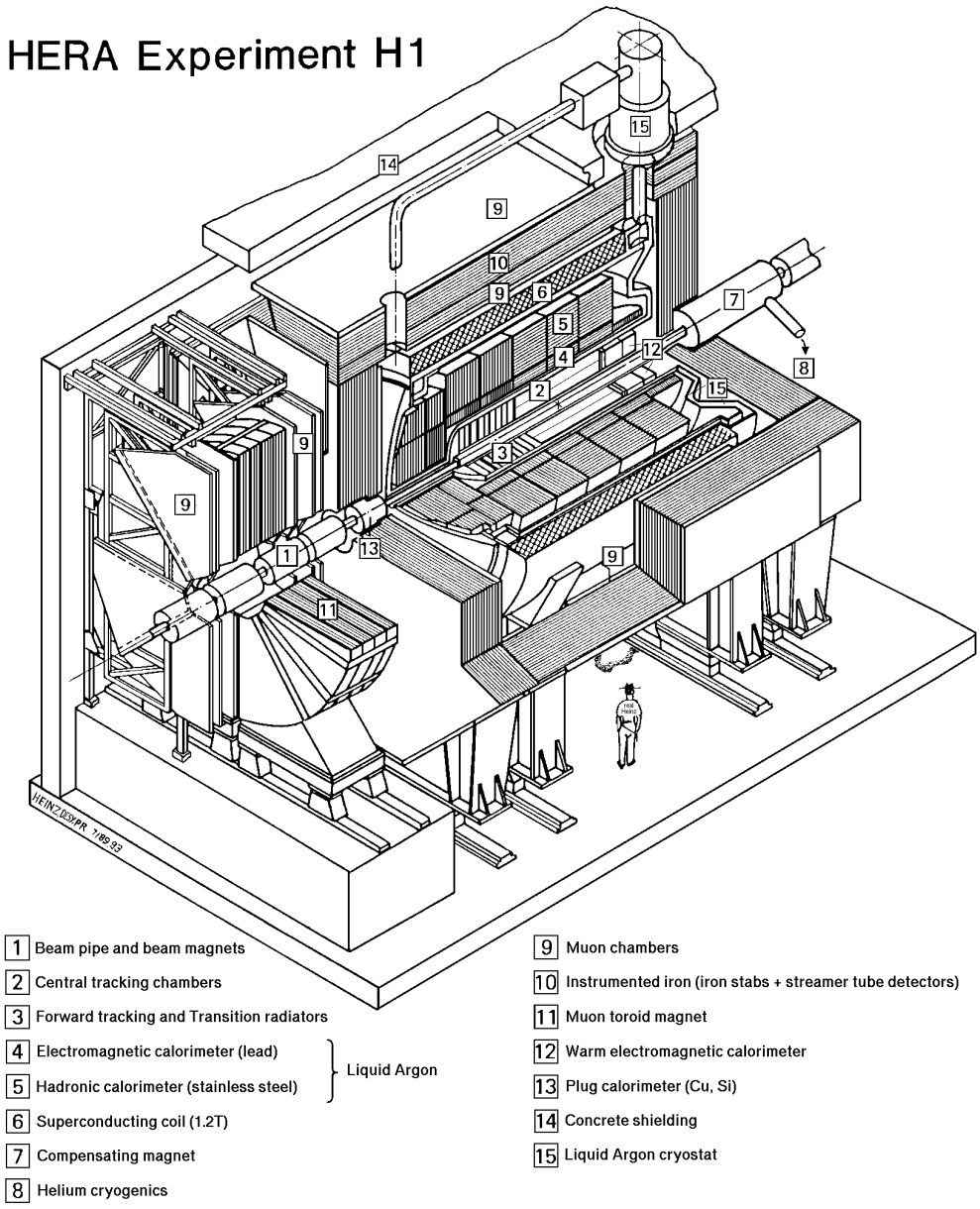

Figure 2.1: *Cross-section of the H1 detector.*

2.2.1 Measurement of Particle Trajectories

Tracking detectors used to detect positions along the trajectories of charged particles are all based on the fact that charged particles have the ability to ionize a medium and that this ionization can be detected. This can be done in two different ways, either by collecting the total ionization products on electrodes using an electric field, or by making the ionization tracks visible in a direct way. Examples of the first method are proportional chambers and drift chambers, whereas an example of the second method is the more old fashioned bubble chamber. A large number of position measurements results in an accurate determination of the particle trajectory. Having a tracking system located inside a magnetic field, the charged particles are bent, and depending on the momentum of the particle the curvature of the track is different. This is used to determine the momentum of charged particles.

A **proportional chamber** is a gaseous detector. When a charge particle passes the gas it ionizes the gas atoms along its trajectory and create pairs of electrons and ions. The electrons drift towards the anode wire, and in the vicinity of the wire the field gradient increases, such that the ionization power of the electrons increases. Therefore the electrons will create an increasing number of new electron-ion pairs, as their distance to the anode decreases. This leads to a chain reaction, and the so called avalanche of secondary electrons can be detected as a pulse on the anode wire. The positive charged ions, travelling in opposite direction to the electrons, will produce a induced charge at the wire contributing to the signal.

In a **multiwire proportional chamber** (MWPC) one uses many anode wires, located between two common cathodes. Each wire is working as a separate detector, which improves the resolution in time and space. The spatial resolution is given by the distance between the wires.

Another tracking device is the **drift chamber**. It works according to the same principle as above, but uses the information, that the created secondary electrons take some time to drift from their production point to the anode. Knowing the drift velocity in the chamber gas and measuring the drift time a spatial resolution much better than for the MWPC can be obtained.

Although the spatial resolution of a drift chamber is better than that of the MWPC, the response time is longer. Therefore the MWPC normally can be used for providing a trigger signal, whereas the drift chambers are used for accurate position measurements.

2.2.2 Detection of Energy, Calorimetry

A calorimeter is a detector that absorbs the total energy of a particle and converts it into a measurable signal. For a good measurement all the primary energy is deposited in the calorimeter. The calorimeter can detect both charged and neutral particles. The energy deposition of the incoming particle occurs by interactions with the detector material such that secondary particles are produced. The secondary particles in turn also interact with the absorbing material and produce new particles. When the secondary particles have reached an energy smaller than a critical energy they are absorbed by the active material.

Different types of calorimeters have different active materials and are therefore detecting different kinds of particles. Since the electromagnetic showers, i.e. showers created by electrons or photons, differ from hadronic showers, one uses different devices for detecting electromagnetic and hadronic activity. Usually the energy resolution is worse for hadrons than for electrons. The calorimeter naturally has to be the last detector in the detector process since the detected particles are totally absorbed, except for muons that have a low ionization capability. The muons are not absorbed, and therefore a typical signature of a muon is a particle that is able to traverse all material of the calorimeter and reach the muon detectors positioned outside the calorimetry system.

2.2.3 Transition Radiation

The transition radiation detector, which is used in H1, is one example of a detector using radiative methods for particle identification. When a high energetic charged particle travels from one medium to another transition radiation occurs if the two mediums have different dielectric properties. The energy of the radiated photons is in the X-ray region. The phenomenon is used to identify particles at energies where other methods, e.g. time of flight measurements, cannot be used. For example one can distinguish high energy electrons and pions by studying the energy spectrum of the radiated photons. A device to detect transition radiation is simply called a transition radiator. [3]

2.3 Tracking in H1

The tracking system of the H1 detector consists of the central tracking system, the forward tracking system and the backward tracking system. These systems in turn constist of other subsystems. The complete tracking system has a full azimuthal coverage and covers the range of polar angles $5^o < \theta < 178^o$. The small regions in the polar angle that are not covered are due to the holes where the beam-pipe enters the detector. A r-z view of the full tracking system can be seen in fig. 2.2.

2.3.1 Central Tracking

The central tracking system is seen in fig. 2.3. It consists of two large concentric drift chambers (CJC1 and CJC2), which each has a length of about 2 meters. These two chambers have wires parallel to the beam-pipe, which gives a good spatial resolution in (r-ϕ). CJC2 is surrounding CJC1. The resolution in z-direction is provided by charge division, i.e. a comparison of the pulse hight of the signal at the two ends of the signal wire give information on the z-position with an accuracy of about 1% of the wire lenght. Two additional chambers, which have wires perpendicular to the beam-pipe, improves the resolution in z. The first z-chamber is positioned between the beam-pipe and CJC1 and the second is positioned between CJC1 and CJC2. The central tracking system also has two MWPCs, sandwiching the CJC1 and the z-chambers. They improve the time resolution to $\sim$ 20 ns. This can be compared with the time between the bunch crossings, $\sim$ 96 ns.

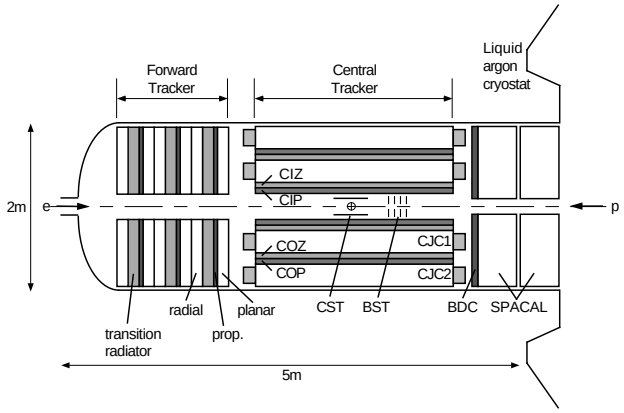

Figure 2.2: *y-z view of the H1 tracking system, which different parts are described in the text. The electron beam and the proton beam are indicated in the figure. In the figure also the Spaghetti Calorimeter (SpaCal) is drawn.*

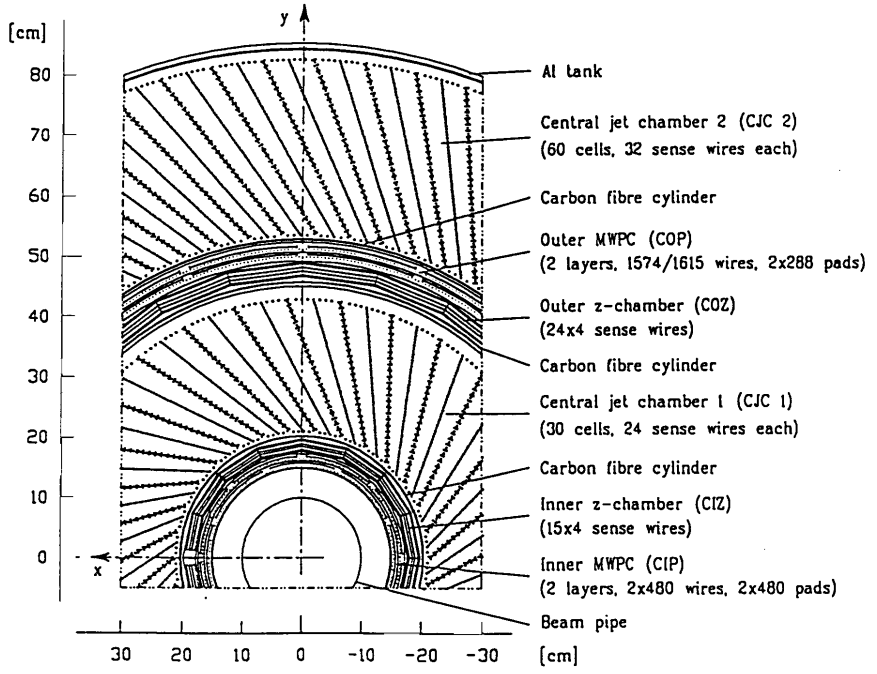

Figure 2.3: *r-ϕ view of the central tracking system.*

2.3.2 Forward and Backward Tracking

Three identical modules are used in the **forward tracking system**. Each module consists of a planar drift chamber, a radial drift chamber, a proportional chamber and a transition radiator.

Since the scattered lepton goes in the backward direction and one wants to determine the scattering angle as well as possible, the **backward tracking system** is constructed such that the resolution of the polar angle is optimized. This is done by having the wires in the backward drift chamber (BDC) running perpendicular to the beam axis, so that the drift direction in the cells is radial.

The electron looses some energy in dead material before it reaches the BDC and the backward calorimeter. However, it has been shown that the particle multiplicity measured by the BDC is proportional to the energy loss in the dead material. This information is used to improve the energy measurement of the scattered electron [6].

2.4 Calorimetry in H1

2.4.1 The Liquid Argon Calorimeter (LAr)

The LAr calorimeter is a sandwich type detector with layers of absorber material and liquid argon as active material in between. The incoming particle interacts with the absorbers creating a shower of particles. The shower is then producing ionization in the liquid argon which is detected by pads on an electronic board. Liquid argon is an inert gas having a high atomic density, which results in large absorbation of the incoming particles. Using the heavier inert gas xenon would result in better absorbation. However, xenon is much more expensive than argon. The spatial resolution in the calorimeter is set by the properties of the pads, i.e. the size of the pads, the distance between the pads, etc.. The more pads the better resolution to the first approximation. Normally the number of pads are limited by the cost of the read out electronics. The design of the cells in the LAr is optimized to allow good spatial resolution, whereas the energy resolution is limited to about $10\%/\sqrt{E}$ for the electromagnetic part and to about $50\%/\sqrt{E}$ for the hadronic part of the detector.

The LAr covers the full azimuthal region and a similar polar angle range as the tracking system. It is located inside the solenoid coil, to decrease the amount of dead material in front of the system and thus to improve the energy resolution. It is contained in a cryostate, to keep the argon liquid. The LAr is segmented into eight wheels, each divided into an electromagnetic part and a hadronic part. For the electromagnetic part, few millimeter thick lead plates are used as absorbers, and for the hadronic part thicker steel absorbers are used. In both cases liquid argon is used as active material. A (r-z) view of the LAr is shown in fig. 2.4.

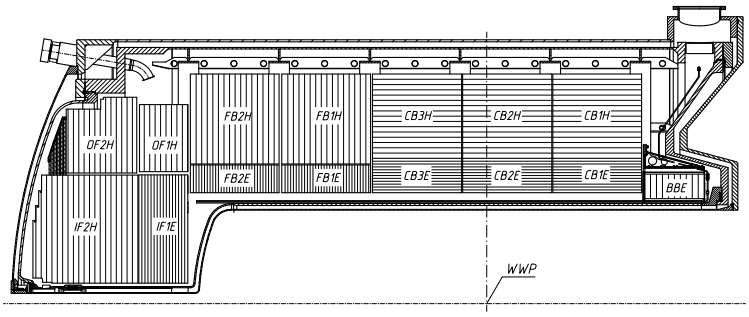

Figure 2.4: *(r-z) view of the upper half of the LAr calorimeter. The beam-axis is drawn as a dashed line, and the interaction vertex is denoted by WWP.*

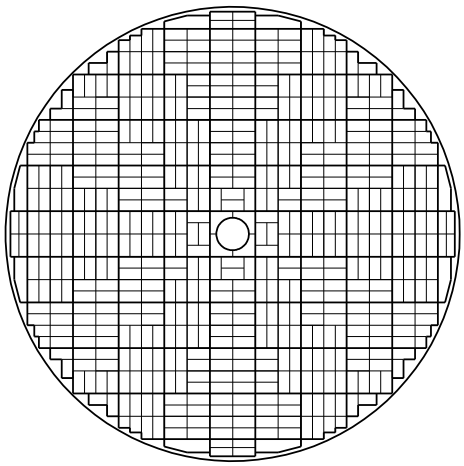

Figure 2.5: *(r-ϕ) view of the electromagnetic part of the SpaCal calorimeter. Each cell, separated by thin lines, has an own photo multiplier.*

2.4.2 The SpaCal

In 1994 the electron detection system in the backward direction, was upgraded by installing the Spaghetti Calorimeter (SpaCal), visible in figure 2.2. It improved the resolution of the electron energy and the electron angle compared to the previous detector. The SpaCal is the main system for the detection of the scattered electron in the lower range of momentum transfer, $1 < Q^2 < 100$ GeV^2. The SpaCal is divided into an electromagnetic part and a hadronic part. The absorbing material in both cases is lead. Showers created in the lead sheets cause scintillating fibers to create light, which is collected by photo multipliers at the end of the fibers. The difference in the size of electromagnetic and hadronic showers is reflected by the size of the calorimeter cells, the thickness of the absorbers, and the diameter of the scintillating fibres. Except for that, the principle of the electromagnetic and the hadronic part is the same.

2.5 Rapidity Gap Detection in H1

For later use we already now define the quantity rapidity, y, as

$$y = \frac{1}{2} \ln \frac{E + p_z}{E - p_z} \tag{2.1}$$

where E is the energy and p_z longitudinal momentum of an object. We see that the shape of y is invariant under longitudinal boosts. In the case there is no particle identification the measured particles are treated as massless, and therefore the rapidity is approximated by the pseudo-rapidity, η.

$$y \approx \eta = -\ln \left(\tan \left(\frac{\theta}{2} \right) \right) \tag{2.2}$$

η is a good way of expressing the polar angle, θ, in the incoming proton direction, since it is opening up the region close to the beam-pipe, where the activity is large.

A special kind of electron-proton scattering is called diffractive scattering. In diffractive scattering the interaction occurs with a colorless object in the proton, and the proton does not break up. The absence of a color field between this object and the rest of the proton means that no hadrons will be produced in the flight direction of the proton. One signature is thus a region in the forward rapidity range where no energy is deposited or no hadronic final states are observed. This is called a rapidity gap event. For the identification of diffractive scattering it is therefore important to have good detector coverage in the forward region. Here follows a short description of the forward muon detector and the proton remnant detector. Rapidity gaps and diffractive scattering are described more detailed in section 3.6. More about how diffractive events are selected, is described in section 4.3.

2.5.1 The Forward Muon Detector and the Proton Remnant Tagger

The **forward muon detector** (FMD) is situated on the outside of the iron yoke of the main detector, and contains a toroid magnet for momentum measurements. It consists of six double layers of drift chambers, three on each side of the magnet, and covers the polar angle $3^o < \theta < 17^o$. Its main task is to detect muons, but it can also be used as a veto detector for forward activity, as done in the identification of diffractive events.

The **proton remnant tagger** (PRT) is situated around the beam-pipe 24 m from the interaction vertex. It is a seven layers scintillator detector, where each layer consists of a scintillator, a light guide and a photo multiplier. The large distance to the interaction point makes the PRT covering small angles. This is important for identification of diffractive protons. The organization of the scintillator layers are shown in fig 2.6. Also the PRT is used as a veto detector.

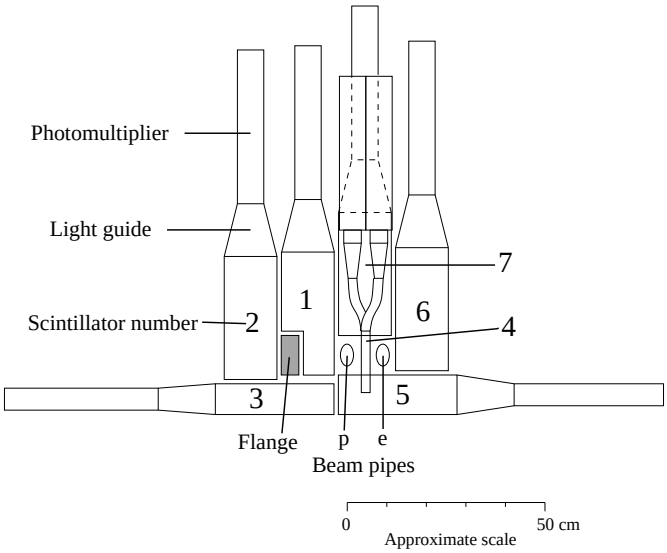

Figure 2.6: *r-ϕ view of the PRT.*

Chapter 3

Deep Inelastic Scattering

3.1 Parton Dynamics and DIS

In 1969 Richard Feynman stated that the nucleon consists of smaller constituents, the partons. He was not the first to do this, but he was the first to do it on the bases of quantum mechanics or, more precisely, on the bases of field theory. It was then up to the experimentalists to determine the properties of the partons and the way they contribute to the structure of the proton. This is one of the main purposes of the H1 experiment. When Feynman lectured he often was asked whether the parton was equivalent to the quark. He answered that it was for the experiments to decide if the fundamental constituents carried fractional charge or not [7]. Today we know, according to the SU(3)-theory and well performed high energy physics experiments, that the quarks could be identified as partons. But the commonly known three valence quarks are not enough to describe the proton structure. In fact, it turns out that the "three quark"-proton model is a naive and old picture of the proton. One also has to consider that virtual quark-anti-quark pairs, called sea quarks, can be produced from the vacuum according to Heisenbergs uncertainty relation, eq. (1.1). According to the conservation laws of quantum numbers the properties of the proton will not change under the sea quark production. Dealing with the structure of the proton also the exchange-particles of the strong force inside the proton has to be considered. These exchange-particles, called gluons, keep or "glue" the quarks together. Quantum fluctuations producing the sea-quarks take place by radiation of gluons, as can be seen in fig. 3.1. In later papers Feynman replaced "partons" by "quarks and gluons".

In processes called Deep Inelastic Scattering (DIS) performed at HERA the accelerated electrons are used to probe the accelerated protons. The advantage of using electrons as probes is that they, as far as we know, are point-like particles and that they interact electromagnetically, which means that the scattering process can be exactly described by the well founded theory of quantum electrodynamics (QED). According to this theory the electron and the proton are interacting through the exchange of a virtual photon. In the end the DIS reaction can thus be seen as a photon-proton scattering, where the photon is used as a probe. The resolving power of the photon is determined by its wave length. To resolve the proton and its structure, the wave length of the photon has to be smaller than

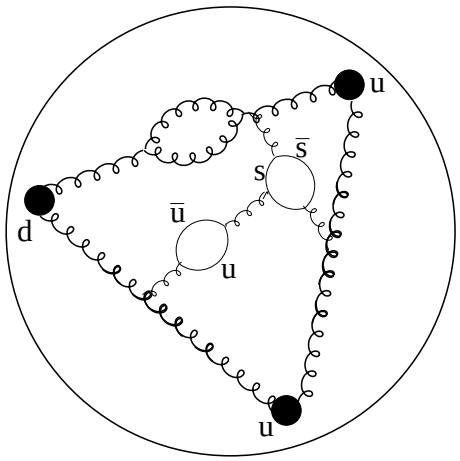

Figure 3.1: *A sketch of a proton, showing the self coupling property of the gluons, and the creation of sea-quarks as quantum fluctuations. The valence quarks are drawn as black dots, whereas the sea-quarks are drawn as lines.*

the dimension of the proton, which makes the energy transferred by the photon so large (using $E = h/\lambda$) that the proton, in almost all cases, will break up. This is deep inelastic scattering.

3.2 DIS Kinematics

A deep inelastic process is described by the Lorentz invariant quantities Q^2, x, y, s and W^2. Let q be the four-momentum of the photon, P_p and P_e the four-momenta of the proton and the incoming electron respectively and P'_e the four-momentum of the scattered electron, as in fig. 3.2, where also Q^2, x, y, s and W^2 are indicated. Then we can define

$$Q^2 \equiv -q^2 = -(P_e - P'_e)^2 \tag{3.1}$$

as the four-momentum transferred from the electron to the photon squared,

$$W^2 \equiv (P_p + q)^2 \tag{3.2}$$

as the hadronic center of mass energy squared and

$$s \equiv (P_e + P_p)^2 \tag{3.3}$$

as the total electron-proton system center of mass energy squared.

The Bjorken x is defined as

$$x \equiv \frac{Q^2}{2P_p \cdot q} \approx \frac{Q^2}{Q^2 + W^2} \tag{3.4}$$

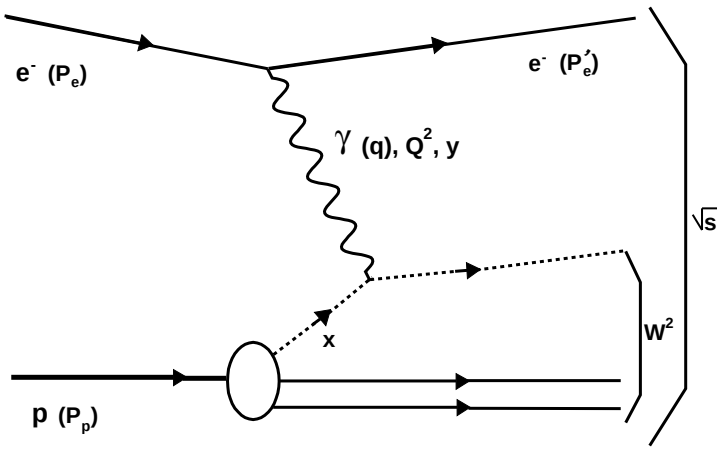

Figure 3.2: *Diagram of a simple DIS-reaction, $ep \rightarrow e'X$, illustrating the kinematic variables.*

and the variable y, which is equivalent to the scaled photon energy, is defined as

$$y \equiv \frac{P_p \cdot q}{P_p \cdot P_e} \tag{3.5}$$

The variable Q^2, defined as the negative invariant mass of the photon squared, is also called the virtuality of the incoming photon. Since $|q| = \frac{1}{\lambda}$, where $\hbar = c = 1$ by convention, Q^2 can be interpreted as a measurement of the resolving power of the photon. It is well known, that to resolve an object one needs a wavelength of the probe that is in the same order as, or smaller than, the spatial extension of the probed object. Hence, the region where $\lambda = \frac{1}{|q|} \ll r_{\text{proton}}$ defines the kinematic region of DIS. This region can, using $r_{\text{proton}} \sim \frac{1}{m_{\text{proton}}}$, also be defined as $Q^2 \gg m^2_{\text{proton}}$, which implies that the energy of the photon is so large that the proton nearly always is fragmented.

If the proton mass is neglected, Q^2 is related to the energies of the incoming (E_e) and the scattered (E'_e) electron, and the electron scattering angle, θ_e[1], by

$$Q^2 \approx 2E_e E'_e(1 + \cos\theta_e) \tag{3.6}$$

The invariant mass of the electron-proton system squared, s, is equivalent to the center of mass energy squared. In a similar way (if one excludes the electron) W^2 is the invariant mass the photon-proton system squared, which is equivalent to the mass of the final state hadronic system squared.

For reactions where the photon interacts directly with a parton in the proton[2], without further parton radiation, the Bjorken scaling variable x can be interpreted as the momentum fraction of the proton carried by the struck parton. In a similar way y can be

[1]For the definition of the polar angel at H1, see section 2.1

[2]Called interactions of lowest order in the strong coupling constant, α_s.

interpreted as the fraction of electron momentum transferred to the photon in the rest frame of the proton. Using $W^2 \gg Q^2 \gg m_p^2$ and eq. (3.4), we see that for high energy DIS we are in the **low x-region**, where $x \ll 1$.

By, writing y as

$$y = \frac{P_p \cdot (P_e - P_e')}{P_p \cdot P_e} \approx 1 - \frac{E_e'(1 - \cos\theta_e)}{2E_e} = 1 - \frac{E_e'}{E_e}\sin^2\left(\frac{\theta_e}{2}\right) \tag{3.7}$$

and rewriting the trigonometry in eq. (3.6), we can relate Q^2 to the transverse momentum of the electron, $p_{\perp,e}$, in the electron-proton laboratory frame and to y by

$$Q^2 \approx \frac{E_e'^2 \sin^2\theta_e}{\frac{E_e'}{E_e}\sin^2\frac{\theta_e}{2}} \approx \frac{p_{\perp,e}^2}{1-y} \tag{3.8}$$

where the polar coordinate form of the transverse momentum has been recognized.

The relation

$$Q^2 \approx xys \tag{3.9}$$

is valid if the proton mass, again, is neglected.

The typical distribution of x, y, Q^2, E_e' and θ_e for the data events used in this analysis are shown if fig. 6.2.

In the following DIS Feynman diagrams the incoming electron will be denoted by the upper straight line and the incoming proton will be denoted by the lower, as in fig. 3.2. Gluons and photons will be drawn in the conventional way, and quarks will be drawn as straight lines. The evolution in time is by convention always from left to right.

3.3 Jets and Hadronization

The strong force is acting between particles carrying colour charge. A single quark or any other coloured object has never been observed in a detector. Obviously, before the quark reaches the detector it has created colourless particles together with other quarks or anti-quarks. If no other quarks are around they will be created in the *hadronization process*. The produced colourless particles are hadrons and this process is hence called hadronization. The hadronization process itself is not very well described theoretically and therefore one has to use phenomenological models. One successful hadronization model is the Lund string model [8], where the connection between the partons is described by a so called colour string.

In a DIS process a large amount of the transverse energy is transferred to one of the partons in the proton. As a consequence this parton will be removed from the other partons in the proton and a colour field is stretched out between them. According to QCD the strong force between the quarks is proportional to the distance between the quarks, and since $E = F \cdot r$ the energy between the quarks will increase with the distance between the

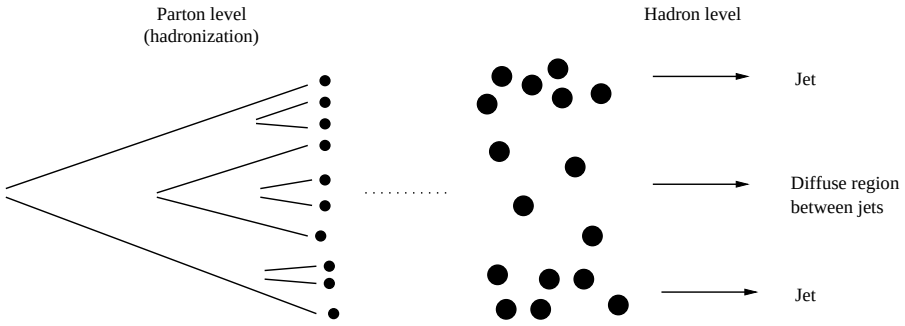

Figure 3.3: *Schematic view of a hadronization process.*

quarks. Furthermore, Einstein postulated that $E \sim m$. This means that when the distance between the quarks is large enough new particles can be created. Since the process is a QCD process the produced massive particles will be quarks and according to the conservation of quantum numbers (that also includes colour) the produced quarks have to be produced as quark - anti quark pairs or diquark - anti diquark pairs. In the Lund string model this can be expressed as if the kinetic energy of the partons is transferred to the string, which breaks when the energy of some part of the string is high enough, such the energy in the string is converted into mass in form of quarks. Each of the two new quarks are attatched to the old quarks by the colour string. The colour string is elastic, and described in analogy to an elastic rubber string, where the string is moving faster closer to the ends. Consequently the particle production also is larger at the string ends. Fig. 3.3 shows a simple sketch of a hadronization process.

So, in a high energy collision a large number of hadrons will be produced and reach the detector. Since the hadronic final state has a large complexity, this flow, or spray, of particles often is approximated as one object, a *jet*. A jet is a flow of particles that is collimated in four-momentum space.

There are correlations between the kinematic properties of the original partons and the properties of the created hadronic state (the jet). These correlations are integrated in hadronization models. The hadronization models takes us from the *parton level*, where the dynamics are described by QCD, to the *hadron level* and the jet dynamics. It should thus be possible to gain information about parton dynamics by studying the properties of the jets.

3.3.1 How to Find Jets

Since jets are not well defined hadronic states, which unambiguously can be assigned to a certain parton, one uses *jet algorithms* to define and find jets. Many different jet algorithms exist, here only the CONE-algorithm and the $k_\perp$-algorithm are explained, the algorithms that were used to obtain the jets analyzed in this work.

In the **CONE-algorithm** one defines a cone with radius R in the phase space of rapidity and azimuthal angle, η-ϕ,

$$R = \sqrt{\Delta\eta^2 + \Delta\phi^2} \tag{3.10}$$

One chooses a seed particle, the transverse momentum of which defines the central axis of the cone. The transverse momenta of all particles within the cone are then summed. If the direction of the new momentum vector coincides with the seed one accepts the cone as a proto-jet, else one repeats the procedure with the summed momentum vector as the new seed. When no more proto-jets can be found, proto-jets are combined or deleted, depending on their overlaps and distribution of transverse momenta, such that the transverse energy of the final jets (cones) is maximized.

For the $\boldsymbol{k}_\perp$**-algorithm** distances between proto-jets are measured in relative transverse momentum (p_t) of the proto-jets. For each proto-jet i the quantity $d_{ip} = p_{t_i}^2$ is defined as the distance between the proton remnant and the proto-jet. For each pair of proto-jets, (i,j), one also calculates the distance $d_{ij} = \min(p_{ti}, p_{tj})R_{ij}^2$, where R_{ij} is the distance between the jets in the η-ϕ phase space. The true jets are then constructed and selected by comparing the magnitude of d_{ip} and d_{ij}. If $d_{ip} > d_{ij}$ the two proto-jets are merged into a new proto-jet according to a p_t-weighting scheme, else the proto-jet i is closest to the proton and becomes a true jet and is not treated anymore. The procedure is iterated until no more proto-jets exist.

3.4 The "$ep \to e'X$" - Cross-Section

As mentioned earlier, one main purpose of DIS is to determine the dynamics of the partons and to understand in which way they build up the proton. This is done by measuring the cross-section of the DIS reaction $ep \to e'X$, where X denotes the final hadronic system, as a function of the kinematic variables defined in section 3.2. The most commonly used variables are x, y and Q^2. The differential cross-section is proportional to the structure functions $F_L(x,Q^2)$ and $F_2(x,Q^2)$, two functions that are independent of each other and include everything about the scattering of a virtual photon with th proton. F_L and F_2 correspond to the scattering of two different polarizations of the virtual photon, longitudinal and transverse respectively. The DIS cross-section is shown in eq. (3.11), where α is the electromagnetic coupling constant.

$$\frac{d^2\sigma}{dxdy^2} = \frac{2\pi\alpha^2}{xQ^4}\Big\{[1+(1-y)^2]F_2(x,Q^2) - y^2F_L(x,Q^2)\Big\} \tag{3.11}$$

The contribution of the longitudinal structure function is small in the kinematic region investigated here, why the transverse is the one that has been mostly investigated. The HERA collider has possibilities to reach regions below $x = 10^{-4}$, and it has been shown that there is a strong rise in F_2 when $x \to 0$.

In the quark-parton model the structure function defines the number of partons carrying a fraction x of the proton momentum as the parton is probed by a photon with a resolving power corresponding to the momentum transfer squared, Q^2.

We now define the *parton density function*, $f_i(x, Q^2)$, which describes the probability of that the parton of type i is carrying the momentum fraction, x, of the proton momentum at a certain value of Q^2. The proton structure function $F_2(x, Q^2)$ can be expressed as the sum over all parton density functions and electric charges, q_i, of the partons in the proton.

$$F_2(x, Q^2) = x \sum_i q_i f_i(x, Q^2) \tag{3.12}$$

The structure function can not be calculated analytically but has to be determined experimentally. As a consequence, looking at eq. (3.11), the DIS cross-section could also not be determined exactly by QCD calculations because the distribution of partons in the proton cannot be calculated from frist principles. For the γ-parton scattering one can use perturbative calculations, where the strong coupling, α_s, is used as the expansion parameter, to calculate the probability of different reactions. The powers of α_s in the expansion corresponds to the number of gluon vertexes in a reaction. In QCD reactions one consequently talks about different orders of the strong coupling constant.

3.4.1 Lowest Order and Order α_s DIS Processes

The fact that the **the lowest order** DIS process does not include any strong coupling means that it is of zeroth order in α_s. In this case the electron-proton collision can be described as purely electromagnetic, and no gluon vertexes exist in the lowest order process. The photon strikes a valence quark inside the proton. The hit quark changes direction and produces a jet, called the current jet, to balance the transverse momentum of the scattered electron. A zeroth order reaction, the so called *QPM process*, is shown in Fig. 3.4

The order α_s QCD process in DIS involves two different reactions, the *QCD Compton* scattering and the *boson gluon fusion* process (BGF) (see fig. 3.5), both including one gluon vertex. The QCD Compton process is analogue to the more known QED Compton process, but instead of an electron emitting a photon (the electromagnetic exchange particle) a quark emits a gluon (the exchange particle of the strong force). In the BGF process the gluon couples to the photon, or vice versa, by a pair creation of quarks. The coupling between the photon and gluon can be calculated analytically with the help of the so called matrix-element, ME, which simply is a bra-ket, $\langle \gamma | V_{ab} | g \rangle$, for the transition between the state a of the photon and the state b of the gluon, or vice versa. The matrix-element is thus the coupling between the purely electromagnetic part and the coloured part of the reaction.

3.4.2 Higher Order DIS Processes

The matrix-elements of QCD processes up to order α_s^2 in DIS have been calculated with perturbative methods. Due to the self-coupling of the gluons and the high energy in the collision, a DIS reaction can produce a complicated system of emitted partons. Calculations up to order α_s^2 are therefore not always sufficient to reproduce the experimental

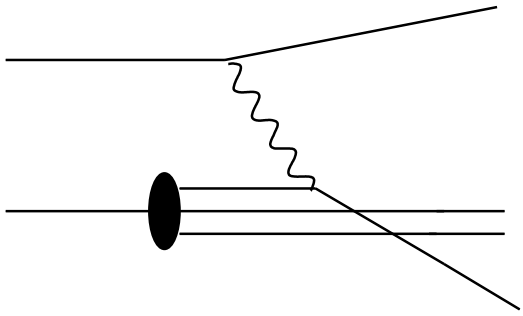

Figure 3.4: *Feynman diagram of lowest order DIS process.*

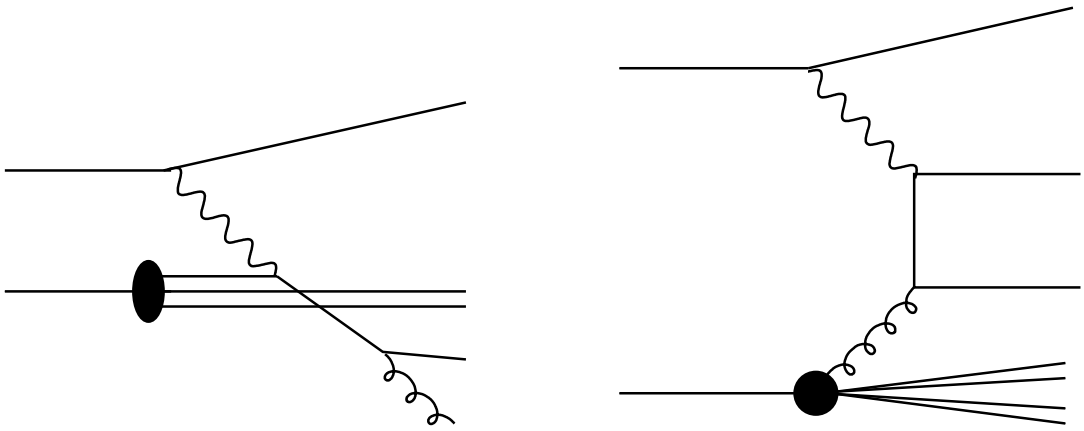

Figure 3.5: *Feynman diagrams of leading order DIS processes, QCD Compton and boson gluon fusion.*

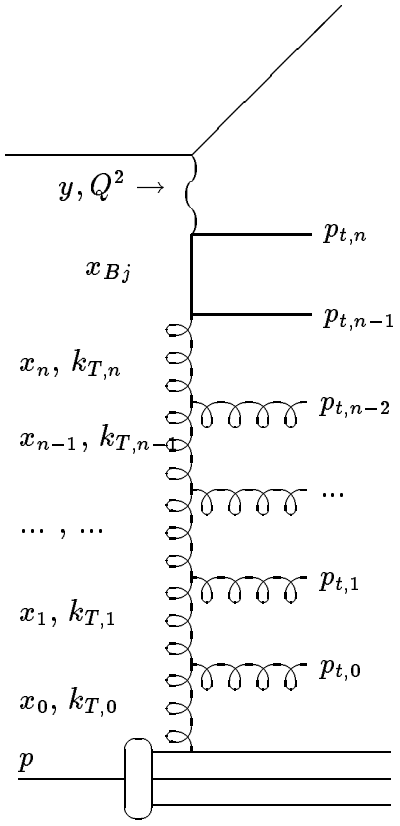

Figure 3.6: *Diagram of a higher order DIS process with a so called parton ladder. The vertex where the photon couples to the quark is referred to as the hard subprocess or the hard scattering vertex. The variables describing the ladder are indicated in the diagram.*

measurement but one also has to include higher order processes. However, the higher order processes are increasingly complicated and processes above order α_s^3 have so far not been calculated. The number of elements in a perturbation matrix increases rapidly for each possible final state, and due to the self-coupling of the gluons the number of reactions and coupling possibilities becomes too large to be contained in a perturbative calculation. One instead calculates and describes the higher order processes by approxiamte methods, called evolution equations. The evolution equation describes the emission of additional gluons by the exchanged gluon in a certain approxiamtion. The probability for such an emission is given by a splitting function defined in the evolution equation. The evolution process leads to a so called gluon ladder between the proton and the hard scattering process described by the matrix-element. Different parton ladders represent different parts of the perturbation series. Cross-sections for higher order processes have been calculated in event generators, e.g. PYTHIA [9], ARIADNE [10], RAPGAP [11], LEPTO [12] and HERWIG [13]. A higher order interaction is shown in fig. 3.6. Here p_t is the transverse momentum of the emitted parton, k_t (also written as $k_\perp$) the transverse momentum of the propagating parton and x the momentum fraction of the propagating mother parton carried by the propagating daughter parton.

For the evolution, one starts at the "bottom" of the parton ladder, with the density function of the parton closest to the proton, f_0, and then apply the evolution equation

to jump one vertex to the next parton with density function, f_1. The basic form of an evolution equation is

$$f_{i+1} = \int f_i \cdot P_i \tag{3.13}$$

where P_i is the splitting kernel, which gives the probability of a vertex to be created. The possible splittings are $g \to gg$, $q \to qq$ and $q \to qg$. Depending on what kind of evolution equation that is used, the variables in P_i are different. One continues the evolution, f_0, f_1, f_2, ..., until the photon, f_n, is reached. Different evolution equations also result in different density functions. Of technical reasons one often uses a backward evolution where one perform the evolution from the hard scattering vertex towards the proton. This is the case for RAPGAP, which is the generator used in the most Monte Carlo studies in this thesis.

3.4.3 DGLAP and BFKL

The DGLAP (Dokshitzer-Gribov-Lipatov-Altarelli-Parisi) [14, 15, 16, 17] and the BFKL (Balitsky-Fadin-Kuraev-Lipatov) [18, 19] evolution equations provide two different approaches for describing the parton emissions. The general perturbative QCD expansion of the cross-section consists of terms depending on $(\alpha_s \log Q^2)^n$ and terms depending on $(\alpha_s \log \frac{1}{x})^n$. DGLAP and BFKL take different terms into consideration. This is done by using different parton dynamics, i.e. different splitting dynamics resulting in different density functions.

The **DGLAP-equation** describes the evolution of the parton densities with Q^2, i.e. the evolution is done in the variable Q^2 or more correct in $\log Q^2$. The requirement for the DGLAP evolution is strong ordering in virtuality of the propagating partons

$$Q^2 \gg k_n^2 ... \gg k_1^2 \gg k_0^2 \tag{3.14}$$

where Q^2 as usually is the virtuality of the exchanged photon, n denotes the parton closest to the hard scattering vertex and 0 is the parton closest to the proton in the parton ladder, as in fig. 3.6. There is also a weak ordering in x, since a parton has to carry smaller momentum than its mother.

Since the DGLAP-equation does not consider terms in $\log \frac{1}{x}$, the DGLAP-equation should not be valid when $x \to 0$, but when $\log Q^2 \gg \log \frac{1}{x}$.

The **BFKL-equation** is valid in the region where x is small enough, such that the $(\alpha_s \log \frac{1}{x})^n$-terms becomes more important than the $(\alpha_s \log Q^2)^n$-terms. When the BFKL-equation is applied, the evolution is made in x (the momentum fraction of the mother parton carried by the daughter parton), and no ordering in virtuality is required in the parton ladder. Instead strong ordering in x is required.

$$x_{Bj}^2 \ll x_n^2 \ll ... \ll x_1^2 \ll x_0^2 \tag{3.15}$$

where Bj denotes the parton closest to the hard scattering vertex (this is the Bjorken x defined in section 3.2), n the parton coupling to the quark pair and 0 the parton closest to

the proton, as in fig. 3.6. The BFKL should thus be valid in the low-x region, unfortunately a region which not is well defined.

The BFKL equation is written as

$$\frac{df(x,k_{\perp,i})}{d\log\frac{1}{x}} = \int dk^2_{\perp,i-1} K(k^2_{\perp,i}, k^2_{\perp,i-1}) f(x, k_{\perp,i-1}) \tag{3.16}$$

where K is the splitting kernel (analogue to P in eq. 3.13) and f is the unintegrated gluon density related to the integrated gluon density in the proton, $g(x,Q^2)$, by

$$xg(x,Q^2) \approx \int_0^{Q^2} dk^2_\perp \frac{1}{k^2_\perp} f(x,k_\perp) \tag{3.17}$$

A characteristic property of BFKL is the random walk behavior of the virtuality, which is a consequence of the fact that no $k^2_\perp$-ordering is required. Just as for any random walk, the $k_\perp$-random walk has a "diffusive" behavior. This can lead to theoretical difficulties since the virtuality can diffuse into a region where perturbation theory can not be applied.

Due to the increasing importance of the $(\log(\frac{1}{x}))^n$ terms at low x, the structure function is not expected to be described by the DGLAP dynamics in this region. However, in the so far measured kinematical region at HERA it is. In order to become more sensitive to BFKL dynamics in the present available region, it is therefore not enough to study inclusive processes. The DGLAP-phase space can be suppressed by measuring specific hadronic final states, where also the $k^2_\perp$-diffusion can be suppressed.

In the measurement of forward jet production the phase space for DGLAP evolution can be suppressed by specific kinematic cuts and thereby the sensitivity for BFKL effects increases. This is also a hadronic final state where the $k_\perp$ diffusion is suppressed. The cuts for suppressing the DGLAP-phase space are described in section 4.2.

3.5 The Resolved Photon

Treating the photon as a point like particle does not always give a correct description of the data. It has been shown [20], and it will be shown here, that for forward jets studies, one also has to consider contribution from resolved photons, i.e. treating the photon as if it contains partons. Otherwise the theory (Monte Carlo) will not agree with the data. The partonic structure of the photon can be explained as in fig. 3.7, where a parton density occurs "in" the photon by pair creation of a quark-antiquark pair, in analogy to the pair creation of an electron-positron pair. The important difference between the two pair creation reactions is that in the strong pair creation the self coupling of the gluons comes into the game. The structure function of the photon has been investigated, but not as well as the proton structure function. In the resolved photon model, the partons of the photon interacts either in a bound state, as a vector meson, or as decoupled partons. [20]

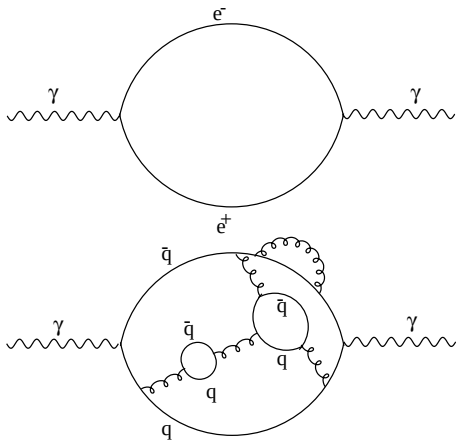

Figure 3.7: *An illustration of the resolved photon, by using the normal electromagnetic pair creation as an analogy.* ***Upper:*** *Pair creation, the photon splits up in an electron-positron pair.* ***Lower:*** *The photon splits up in a quark-antiquark pair, leading to a higher order resolved photon, such that the photon can be treated as an object with a partonic structure. The lower figure can be compared with fig. 3.1, where the parton structure of the proton is illustrated.*

3.6 Diffractive DIS

Diffractive scattering is characterized by the absence of colour flow between the proton and the rest of the DIS system. The exchanged photon interacts with a colour-less object inside the proton in contrast to a "normal" scattering where the photon interacts directly with one of the partons of the proton. This also involves that the proton is not part of the normal fragmentation process. Instead the proton remains intact, and essentially proceeds unscattered in the very forward proton direction. An alternative is that the proton dissociate, that means that the proton after the diffractive scattering fragments, outside the beam-pipe, into a state with a mass larger than the proton mass. In diffractive proton dissociation the proton is still separated from the rest of the system. A class of DIS events is due to diffractive scattering, and are therefore called diffractive DIS. At HERA about $5 - 10\%$ of all events are diffractive events.

Due to the lack of colour exchange between the hard scattering vertex and the proton diffractive DIS is characterized by a so called rapidity gap between the proton and the current jet, where no hadronic final states or energy flow is observed. A diffractive event is drawn in fig. 3.8. The hadronic final states on each side of the rapidity gap are here called X and Y respectively. In fig. 3.8 the Y-system consists of the scattered proton only. However theoretically the exchange of the Pomeron can be positioned on other places in the parton ladder. In the following Y will denote the scattered proton only.

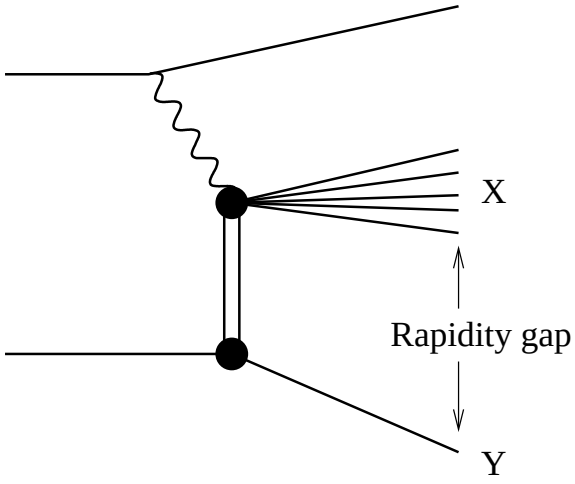

Figure 3.8: *Feynman diagram of a diffractive DIS event, called rapidity gap event. X and Y denote the hadronic final states on respective side of the rapidity gap.*

3.7 Regge Theory and The Pomeron

High energy scattering can in some cases be described by the exchange of so called Regge poles. These are named after Regge who presented a theoretical model in 1960-70 to explain the physics of diffractive scattering.

In a two-body scattering process $A + B \rightarrow C + D$, the Regge theory order resonances and exchange particles in terms of the Mandelstam variables s and t respectively, where s is the center of mass energy squared and t the four-momentum transferred to the exchange particle squared. The variables can be expressed as

$$s = (A + B)^2 = (C + D)^2 \tag{3.18}$$

$$t = (A - C)^2 = (B - D)^2 \tag{3.19}$$

where A, B, C and D are the four-momentum of the various bodies involved in the scattering. This make s and t also to the invariant masses of the resonance and the exchange, respectively, shown in fig. 3.9. s and t are analogue to the variables used to describe the DIS kinematics in section 3.2.

The important quantity in Regge theory is $\alpha(t)$, which is a dimensionless quantity corresponding to the complex angular momentum of the exchanged object at a squared momentum transfer t. In a scattering process t is negative but by continuation of $\alpha(t)$ into the region of positive t values, the poles manifest themselves as real objects. It was proposed that all hadrons including resonances will lie on common trajectories in the $\alpha(t)$-t plane (Regge trajectories). The pole which has $\alpha(0) = 1$ is called the Pomeron whereas all other poles have $\alpha(0) < 1$. The Pomeron has the quantum numbers of vacuum.

If the angular momentum of different exchange particles is plotted as a function of their invariant mass squared, t, the exchanges will lie on a straight line. This is experimentally

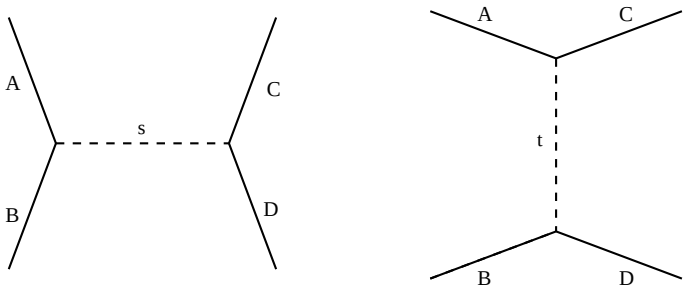

Figure 3.9: *Feynman diagrams of a resonance process (**left**) and an exchange process (**right**).*

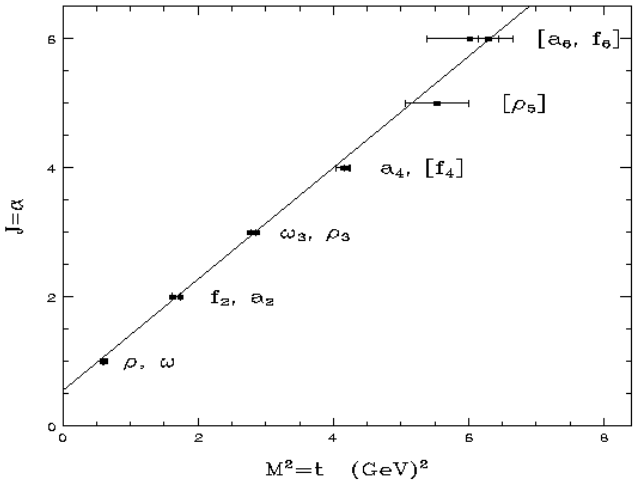

Figure 3.10: *The spin-t correlations for the mesons ω, f, ρ, a, called the meson trajectory. The line is a straight line fit. Note that the mesons are bosons, i.e. spin 1 particles, lying on equal distance on the trajectory.*

shown. In fig. 3.10 [21] the so called meson trajectory is shown, where the spin-t correlation is plotted for mesons. Such trajectories, Regge trajectories, can be expressed as

$$\alpha(t) = \alpha(0) + \alpha' t \tag{3.20}$$

where α is the angular momentum (the spin) of the exchanged particle. This is simply the equation of a straight line, where α' is the slope of the line.

The diffractive scattering can be seen as a two-body process, where the Pomeron is an exchange object. It is experimentally shown that this ansatz gives a good description of the diffractive scattering process and its cross-section. The Pomeron has been measured to give $\alpha_{I\!P}(0) = 1.08$ and $\alpha'_{I\!P} = 0.25$. Contribution of other Regge trajectories than the Pomeron, turn out to be important to describe rapidity gap events in certain regions of phase space. Examples are the Reggeon or the $\pi^{\pm}$ and the π^0 exchange. The difference between these and the Pomeron is the different energy dependences on the momentum fraction of the proton

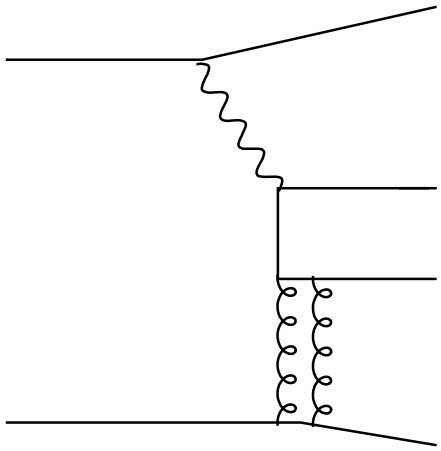

Figure 3.11: *A Feynman diagram of a 2 gluon exchange model*

momentum transferred to the exchange ($x_{\mathbb{P}}$). A short investigation of the contribution of these exchanges to the total diffractive cross-section is done in section 8. The properties of the Pomeron are still not very well known, but diffractive scattering can be used to gain information about the Pomeron. Two different colourless exchange models are presently discussed in diffractive scattering theory, *the resolved Pomeron model* and *the 2-gluon exchange model.*

3.7.1 The 2-gluon Exchange Model

The 2-gluon exchange model is the simplest possible QCD model that satisfies the requirements for a colourless object. The 2-gluon model is a perturbative model. A Feynman diagram of a 2-gluon Pomeron is shown in fig. 3.11.

3.7.2 The Resolved Pomeron

In the resolved Pomeron model the Pomeron is treated as an object with partonic structure. In this case the electron-Pomeron collision is similar to the electron-proton collision, and a structure function for the Pomeron can be defined. This means that the scattering occurs against one of the partons inside the Pomeron and leaves a Pomeron remnant that will fragment into a jet. Also here higher order interactions contribute to the cross-section of the scattering similar to the normal DIS process, e.g. QCD Compton and BGF, or ladder reactions that can be described by DGLAP or BFKL.

3.8 Kinematics of Diffractive DIS

To describe diffractive DIS one has to define the Lorentz invariant variables M_X^2, M_Y^2, t and $x_{\mathbb{P}}$ beyond the common inclusive variables. We denote the four-momenta of the hadronic final states on each side of the rapidity gap by P_X and P_Y respectively, and the four-momenta of the incoming proton by P_p. We define

$$M_X^2 = P_X^2 \qquad M_Y^2 = P_Y^2 \tag{3.21}$$

as the invariant mass of the corresponding hadronic final states squared and

$$t = (P_p - P_Y)^2 \tag{3.22}$$

as the four-momentum transferred to the exchange Pomeron squared, i.e. the invariant mass of the Pomeron squared. t is essentially the same as in eq. (3.19).

$$x_{\mathbb{P}} = \frac{q \cdot (P_p - P_Y')}{q \cdot P_p} = \frac{Q^2 + M_X^2}{Q^2 + W^2} \tag{3.23}$$

is defined as the fraction of proton momentum carried by the Pomeron. $\mathbb{P}$ denotes the Pomeron, but is often referred to as a generic name for any exchange in diffractive scattering.

Chapter 4

Event Selections

Events produced by specific processes are selected by applying cuts on the reconstructed kinematics at detector level, and requiring (or veto) activity in detectors or part of detectors. Different cuts help us to suppress backgrounds, minimize corrections and restrict ourselves to regions where the acceptances of the detectors are reasonable. This leads to good reconstructed kinematic variables.

The events and their kinematics reconstructed from the raw data are collected in data files called "ntuples". In an "ntuple" kinematic information on particle and jet candidates, referred to as objects, are created. An object could be one or several clusters or tracks in a detector. The kinematic variables of the objects, that are needed for the analysis, are thus stored in the "ntuples". The advantage of this is that it is easier and faster to create histograms and to work with the kinematics, e.g. to apply different cuts, in comparison to working directly with the raw data. The analysis in this thesis is done on the same Monte Carlo and data "ntuples" as in [22]. That means that the kinematic reconstruction already is done, and the event selection is left to do. The DIS selection made here is based on [4, 5] and [22]. The forward jet selection is based on [22], and for the methods of the diffractive selection I have used [4, 5]. All the used selections are commonly used within the H1 experiment.

4.1 DIS Selection

In order to select DIS events cuts on the scattered electron (section 4.1.1), the interaction vertex (section 4.1.2) and on the DIS kinematic variables Q^2 and y (section 4.1.4) are made. One also defines a new quantity, referred to as $\sum(E - p_z)$ for the final state, on which cuts are applied (section 4.1.3). The DIS selection, described in this section, constitute the base of the analysed events.

4.1.1 Identification of the Scattered Electron

For DIS processes the scattered electron is detected either in the SpaCal or in the LAr calorimeter. In this analysis only the SpaCal has been used, which means that the scattering angle of the electron, θ_e, has to be within the acceptance of the SpaCal, i.e.

$$156^o < \theta_e < 172^o \tag{4.1}$$

To suppress contributions from scattered electrons which do not originate from the electron beam, one requires a minimum electron energy, E'_e, deposit in the SpaCal.

$$E'_e > 10 \text{ GeV} \tag{4.2}$$

For further noise reduction one also requires a maximum radius of the electron candidate cluster in the SpaCal

$$R_{\text{Cluster}} < 3.5 \text{ cm} \tag{4.3}$$

This prevents noise from hadronic showers, which have a larger spatial extent than electromagnetic showers.

To further prevent hadrons from faking the scattered electron, one also requires that there is no activity in the hadronic part of the SpaCal just behind the electromagnetic electron candidate cluster.

$$E_{\text{Had}} < 0.5 \text{ GeV} \tag{4.4}$$

where E_{Had} is the energy of the hadronic cluster situated behind the electron candidate SpaCal cluster.

Also photons can fake electrons in the SpaCal, but since photons do not produce tracks in the BDC positioned in front of the SpaCal, one requires that the radial distance, ΔR_{BDC}, between a BDC-track and a SpaCal-cluster is less than 3.0 cm. Thus,

$$\Delta R_{\text{BDC}} < 3.0 \text{ cm} \tag{4.5}$$

reduces the background of events with uncorrelated particle tracks and photon showers (faked electrons).

When electrons are scattered in directions close to the edge of the calorimeter it can happen that the full electron energy is not deposited in the SpaCal. Hence, to obtain good energy measurements one defines a "veto"-region where the energy deposit is not allowed to exceed 1.0 GeV.

$$E_{\text{VETO}} < 1.0 \text{ GeV} \tag{4.6}$$

where E_{VETO} is the total energy deposit in the four veto layers, positioned in the SpaCal, closest to the beam pipe. They can clearly be seen in fig. 2.5.

Except for the cuts described above, in Monte Carlo events the generated value of R_{Cluster} is multiplied by 1.065, to obtain a better agreement between the Monte Carlo and the data [22].

4.1.2 The Interaction Vertex

The collisions between the electrons and the protons do not in general occur at the nominal vertex position, i.e. all collisions do not take place exactly at $z = 0$. Instead the collision region is described by a Gaussian distribution around $z = 0$. It is also possible that some beam particles collide with the beam-pipe. To suppress this kind of collisions one requires that the collision occurs within 35 cm from $z = 0$.

$$|z_{\text{vertex}}| < 35 \text{ cm} \tag{4.7}$$

In this region it has been shown that true reactions are dominating.

4.1.3 The Final State $\sum_i (E_i - p_{z,i})$

One defines the quantity $\sum_i (E_i - p_{z,i})$ where i runs over all final state objects including the electron, which for a perfect measurement should be $\sum_i (E_i - p_{z,i}) \approx 2E_e = 55$ GeV. This is a consequence of momentum conservation if one neglects the proton mass and the electron mass, and defines the positive z-direction along the proton direction. In the event selection one requires that

$$35 < \sum_i (E_i - p_{z,i}) < 75 \text{ GeV} \tag{4.8}$$

This cut prevents events with badly reconstructed kinematics to be used.

The lower limit also reduces events with faked electrons (see above) in the SpaCal, where the true electron vanishes in the beam-pipe. This can happen for *photoproduction* events where a real photon is created in place of the otherwise virtual photon, such that $Q^2 \approx 0$ (not treated in this analysis).

4.1.4 General DIS Reconstruction Cuts

In order to constrain the electron within the acceptance of the SpaCal one also applies the cut

$$5 < Q^2 < 85 \text{ GeV}^2 \tag{4.9}$$

where the lower limit assures that only DIS events are selected. Finally the cut

$$0.1 < y < 0.7 \tag{4.10}$$

is applied, where the lower cut suppress photoproduction, but also erase regions where the resolution in y is poor. The upper limit approximately corresponds to the cuts (4.2) and (4.1), which simply can be estimated by using eq. (3.7).

4.2 Forward Jet Selection

Forward jets are those going close to the proton direction. To select these we restrict the rapidity of the jet, $\eta_{\rm jet}$, by the cut

$$1.735 < \eta_{\rm jet} < 2.790 \tag{4.11}$$

The upper limit prevents that a detected fraction of the proton remnant is misidentified.

Activity in the detector which does not originate from the collision (noise) is prevented from being misidentified as forward jets by applying a cut on the transverse momentum of the jet, $p_{\perp,jet}$

$$p_{\perp,jet} > 3.5 \text{ GeV} \tag{4.12}$$

In order to increase the sensitivity to BFKL-dynamics, we apply a specific cut to suppress the phase space for DGLAP evolution. This is achieved by requiring the relative transverse momentum, $\frac{p^2_{\perp,\rm jet}}{Q^2}$ to be approximately equal to 1, i.e.

$$0.5 < \frac{p^2_{\perp \rm jet}}{Q^2} < 2.0 \tag{4.13}$$

This cut makes the virtuality in each end of the parton ladder approximately the same, and no strong ordering in virtuality becomes possible.

Furthermore, the relative energy of the jet, $x_{\rm jet}$, is required to be

$$\frac{E_{\rm jet}}{E_{\rm proton}} \equiv x_{\rm jet} > 0.035 \tag{4.14}$$

where $E_{\rm jet}$ and $E_{\rm proton}$ are the energies of the jet and the incoming proton respectively. The quantity can be compared to the Bjorken x, eq. (3.4), and since we are in the low x region, where a typical value of $x_{\rm Bjorken} \sim 10^{-3}$, the cut requires that the difference between the $x_{\rm Bjorken}$ and $x_{\rm jet}$ becomes large. Since the two x, again, are at different ends of the parton ladder, this leaves room for strong ordering in fractional momentum, i.e. a larger BFKL phase space.

4.3 Diffractive Selection

The diffractive selection is based on cuts that remove events with some activity in the forward going direction. The main cut for this is a cut in $\eta_{\rm max}$, a variable defined as the pseudo-rapidity of the most forward going object in the LAr calorimeter. For noise (see above) reduction one also requires that the energy of the detected object is above 300 MeV. The typical $\eta_{\rm max}$ distribution for diffractive events at detector level has a plateau at low $\eta_{\rm max}$, which derives from the rapidity gap events. The $\eta_{\rm max}$-distribution is plotted in

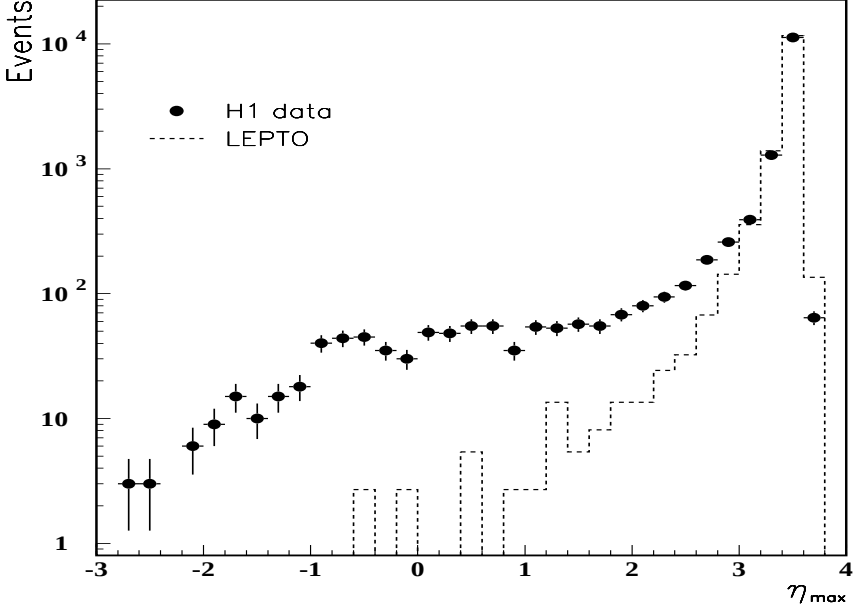

Figure 4.1: *η_{max}-plot where the filled dots represent the data, and standard DIS events, generated by LEPTO, are represented by a dashed line. One sees that normal DIS does not describe the data, one also has to consider diffractive DIS.*

fig. 4.1 with the diffractive and the normal DIS events separated. To reject events without rapidity gaps one requires that

$$\eta_{\max} < 3.3 \tag{4.15}$$

For the diffractive selection the forward muon detector (FMD) and the proton remnant tagger (PRT) are used as veto detectors. For the FMD one requires that

$$N_{\mathrm{FMD}} < 2 \tag{4.16}$$

where N_{FMD} is the total number of hit pairs in the first three layers in the FMD. Requiring zero activity would reject also a large fraction of diffractive events due to the large amount of noise activity.

The noise in the PRT is negligible and one requires that

$$N_{\mathrm{PRT}} = 0 \tag{4.17}$$

where N_{PRT} is the total number of hits in all seven PRT layers.

4.4 Statistical Results of the Selections

In table 4.1 the number of events remaining after different selections are shown. Also the number of two and three forward jet events are shown. The table shows non-corrected, non-weighted data events. The number of events in the table gives a general impression of the effect of various requirements although in the analysis the numbers will be modified due to weighting of the events and corrections of the forward detectors, i.e. the PRT and the FMD.

Additional Requirements	Statistics
None	$\sim 5.1 \cdot 10^6$ events
Electron candidate in SPACAL	$\sim 5.0 \cdot 10^6$ events
DIS Selection	$\sim 5.2 \cdot 10^5$ events
At least one jet in the event	$\sim 5.1 \cdot 10^5$ events
Forward jet selection	$\sim 7.8 \cdot 10^3$ events
Number of 2 forward jets event	~ 170 events
Number of 3 forward jets event	1 event
Diffractive selection	54 events

Table 4.1: *The result of different requirements in order, i.e. requirement of an electron candidate in the SPACAL was applied first and the diffractive selection last. (The diffractive selection is applied on the forward jet selection. Not in addition to the 2 or 3 forward jets.)*

Chapter 5

The Event Display

The H1 event display provides not only an interesting way of visualising events, but is also a good pedagogical tool in order to demonstrate the signatures of different event types. Below follow some examples of events reconstructed and visualized in the event display. In each picture the tracking system, the LAr calorimeter, the SPACAL and the forward muon system are shown. The large box, surrounding the LAr, is the iron yoke of the main solenoid magnet. The yoke consists of thick iron layers with detectors for muon detection in between. The small square plotted over the beam-pipe in the forward direction is the plug calorimeter (PLUG), which is used to detect activity in the very forward region. Unfortunately the PLUG was not working satisfactory during 1997, and could therefore not be used for an improved diffractive selection. The reconstructed tracks are shown as solid lines, and the energy deposition in the calorimeter as filled squares in the figures. In fig. 5.1 two data events are displayed. The upper figure shows a DIS event in which the jet algorithm found two forward jets. The lower figure is an example of a diffractive forward jet event. Notice the much higher activity in the forward region of the LAr for the DIS event. Fig. 5.2 shows the only event in the analysis where three forward jets were found by the inclusive $k_\perp$-cluster algorithm. The event did not pass the diffractive selection.

Also events generated by the RAPGAP event generator can be visualized in the event display. In this case one has the advantage of knowing the generated particle types and their kinematics. One can therefore choose to display only specific particles, like for example only the "tracks" of the photons or only the electrons. Fig. 5.3 shows a diffractive forward jet event for different views and track reconstructions. The tracks are shown for all charged particles (5.3, upper left and upper right), for only the electrons (5.3, lower left) and only the photons (5.3, lower right). Also an (r-ϕ)-view of the tracking system for the charged particles is included in the figure (5.3, upper right), where the electrons are seen as tracks with smaller bending radius than the more massive hadrons. One can notice the typical diffractive scattered proton in the first picture in fig. 5.3, going almost unchanged, straight in the forward direction.

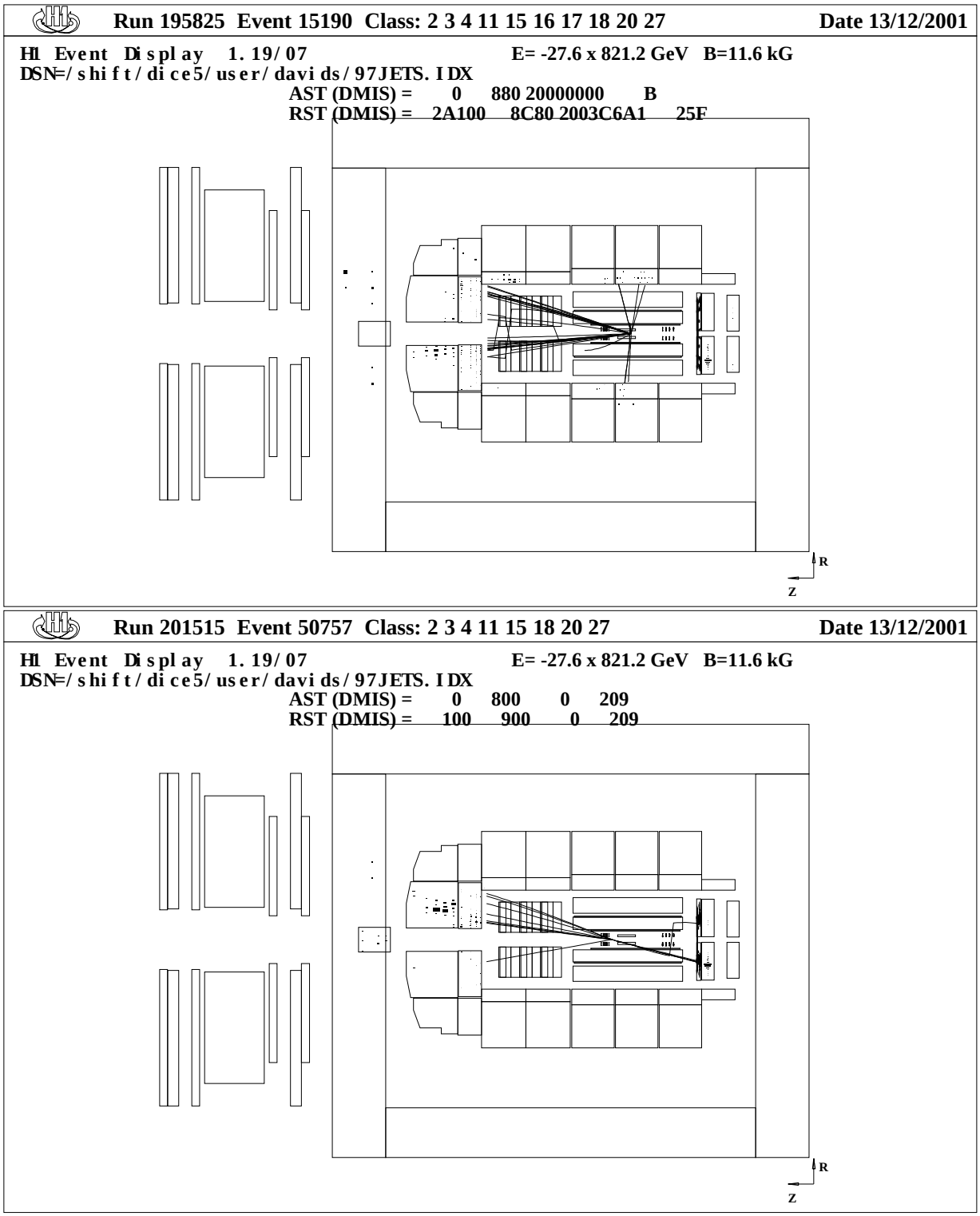

Figure 5.1: *A diffractive (upper) and a diffractive (lower) data event, reconstructed in the event display. The non-diffractive event contains two forward jets. In the SPACAL one can notice the distinct cluster of the scattered electron. The track of the scattered electron in the upper figure is obviously not successfully reconstructed in the event display.*

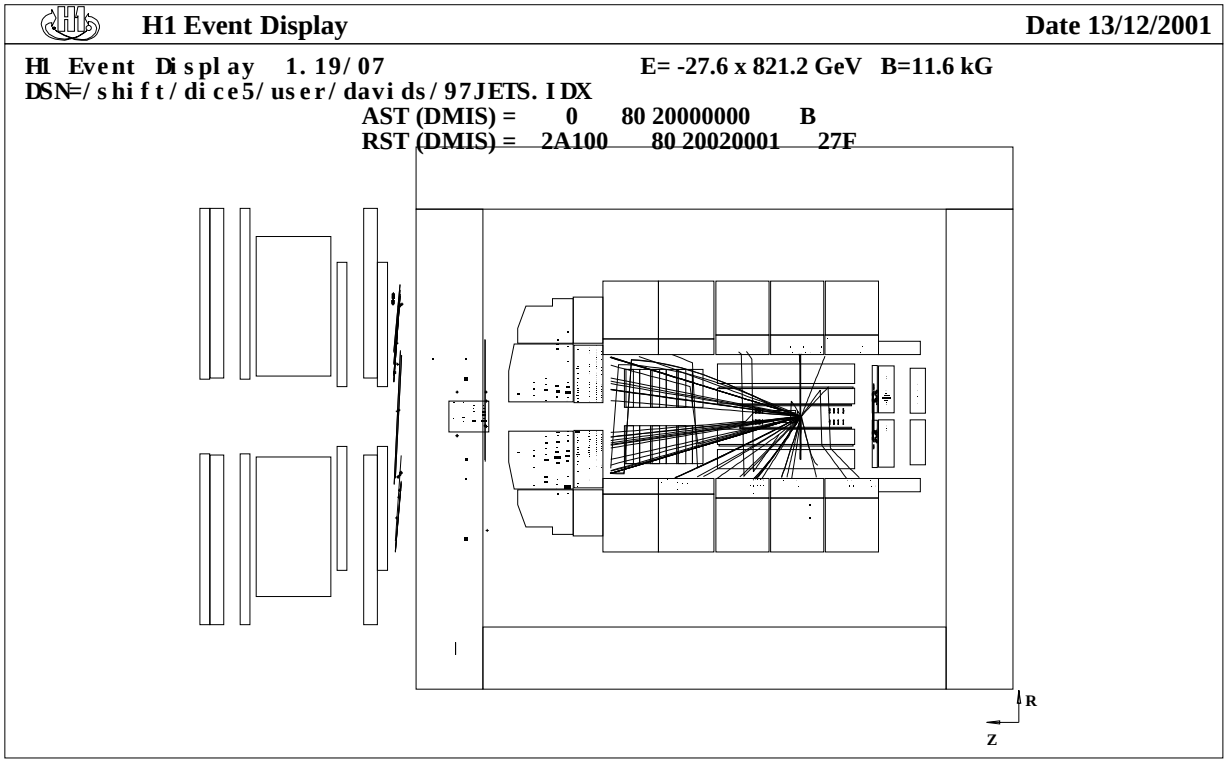

Figure 5.2: *The event display showing the only event in the 1997 data where 3 forward jets were found by the $k_\perp$-cluster algorithm. The event is a non-diffractive event.*

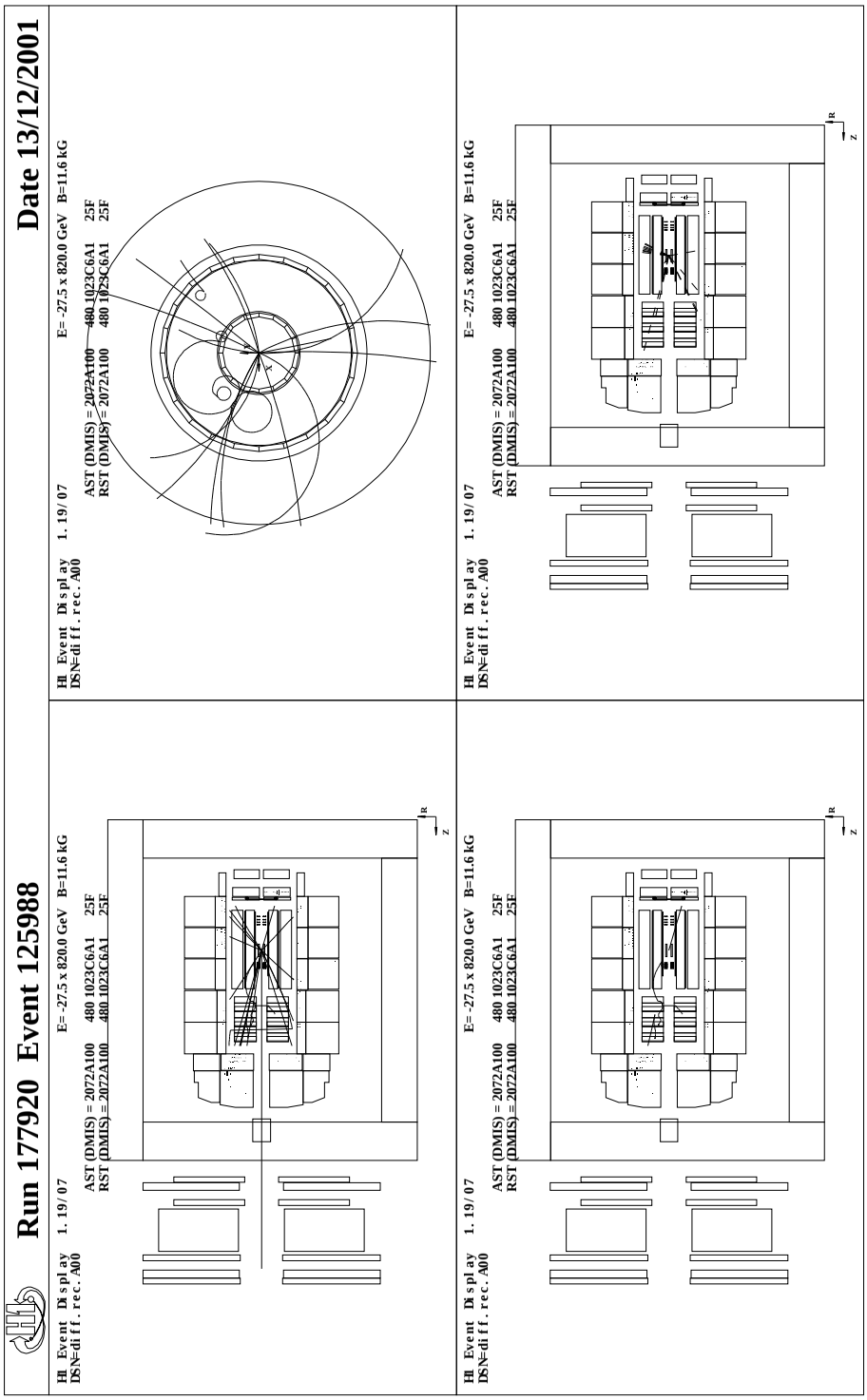

Figure 5.3: *Different views and track reconstructions of a Monte Carlo generated diffractive forward jet event. In all pictures of the drawn LAr the clusters derives from ionizing particles.* ***Upper left:*** *Only reconstructed tracks from charged particles are drawn.* ***Upper right:*** *A (r-ϕ)-view of the tracking system. Only tracks from charged particles are drawn.* ***Lower left:*** *Only reconstructed electron tracks are drawn.* ***Lower right:*** *Event displayed only with the reconstructed photon "tracks".*

Chapter 6

Data-MC Agreement and Forward Corrections

In order to verify that the Monte Carlo generator RAPGAP, which is used to calculate correction factors, reproduce the data in a reasonable way we have made comparisons between data and the predictions for various distributions of kinematic variables. A good agreement in the so called check plots gives us confidence in the result obtained in the analysis.

Here is the so-called *electron method* used to calculate the quantities x, y and Q^2. In the electron method the energy of the scattered electron, E'_e, and the scattering angle of the electron, θ_e, is measured in the SpaCal, the BDC and the LAr calorimeter, and then used to calculate x, y and Q^2.

In fig. 6.1 the typical distributions of the DIS kinematics are shown for data and simulated events that have passed the DIS selection. The histograms are normalized to bin width and number of events, and are thus a shape comparison between data and simulation. The agreement is good. The same distributions are plotted in fig. 6.2 for the events that have passed also the diffractive selection, and also here is the agreement good. A good control of the agreement between the generated events and the data when the forward jet selection is applied is not possible in this way since to few events remain after the forward jet selection.

6.1 Forward Corrections

The quality of the Monte Carlo simulations of the forward detectors are studied by applying anti-diffractive cuts, which simply are cuts that are opposite to the diffractive cuts described earlier, i.e. activity above the noise level is required in the PRT and the FMD, and hadronic final states are required to exist for $\eta > 3.3$. Since some noise and efficiencies in the forward detectors have not been simulated in the detector simulations, one needs to correct for this manually.

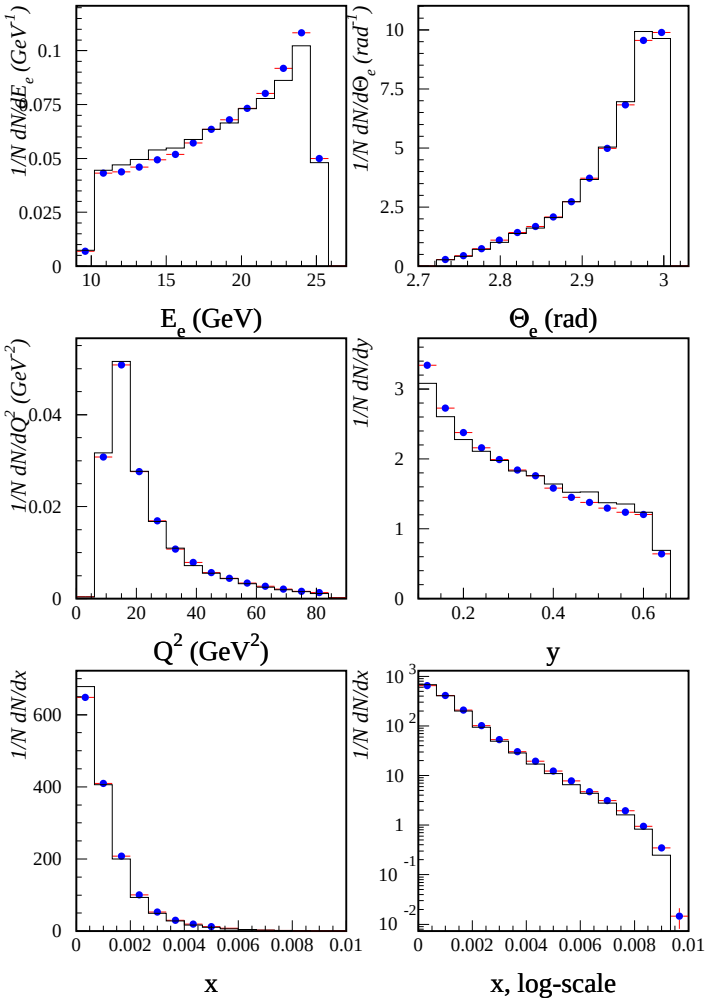

Figure 6.1: *Distributions of some kinematic variables for events that have passed the DIS selection. The data is shown as dots while the simulation is shown as a full line.*

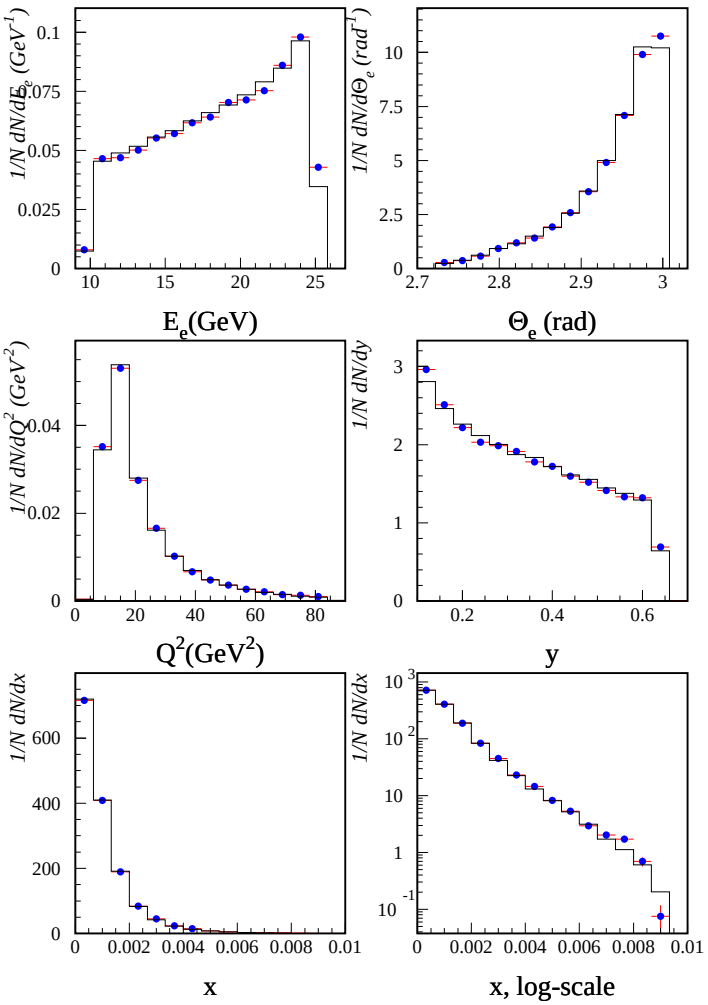

Figure 6.2: *Distributions of some kinematic variable for DIS events that have passed the diffractive selection. The data is shown as dots while the simulation is shown as a full line.*

The efficiency, ϵ_i, for each of the 7 scintillator layers, i, in the proton remnant tagger is defined as

$$\epsilon_i = \frac{N_i}{N_{\mathrm{PRT}}}(N_{\mathrm{FMD}} > 1, \eta_{\mathrm{max}} > 3.3) \tag{6.1}$$

where the anti-diffractive cuts are applied and N_i stands for number of hits in each scintillator and N_{PRT} the number of hits in the full PRT detector. The 7 efficiencies of the PRT are not correctly integrated in the detector simulations. The layers in the PRT are aging fast due to the high radiation level close to the beam, why the efficiency for the data by time gets increasingly worse compared to the efficiency in the simulations. One therefore has to apply a correction factor to each efficiency of the 7 layers in the simulations. In addition to this local correction factors also a global correction was applied. The correction factors are shown in table 6.1. Here the corrections factors from [4] are used, where each local correction is the efficiency in the data divided by the efficiency in the Monte Carlo, whereas the global correction factor is the probability of any activity in the PRT for the data divided by the probability of any activity in the PRT for the Monte Carlo after that the local correction factors have been applied.

Global Scale Factor	0.77

Layer	Local Scale Factor
1	0.4604
2	0.5172
3	1.0000
4	0.1914
5	0.0868
6	0.0954
7	0.2170

Table 6.1: *The global and local corrections for the PRT.*

The large noise activity in the FMD is not simulated in the detector simulations, and one has to add also this manually. This is done by randomly applying noise events taken from the same run year, in this case 1997. The plots comparing data and simulation after the corrections are shown in fig. 6.3.

In this analysis it turned out that using an η_{max} calculated from both detector tracks and detector clusters gave the best result in the anti-diffractive plots. The alternative would be to use an η_{max} calculated from detector clusters only.

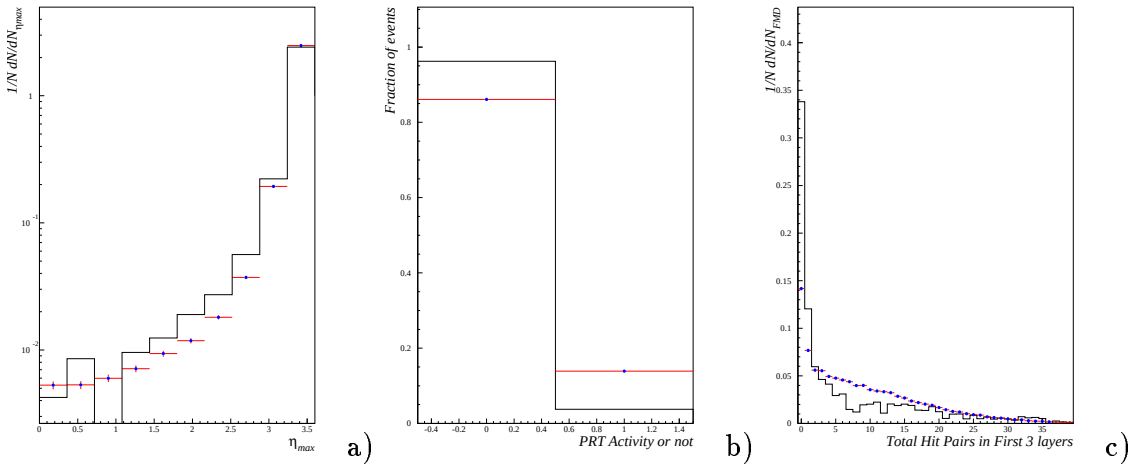

Figure 6.3: *a)* η_{max} *plotted for* $N_{PRT} > 0$ *and* $N_{FMD} > 1$. *b) The activity in the FMD plotted for* $N_{PRT} > 0$ *and* $\eta_{max} > 3.3$. *c) The activity in the PRT plotted for* $N_{FMD} > 1$ *and* $\eta_{max} > 3.3$.

Chapter 7

Forward Jet Studies

In this chapter a short Monte Carlo study of forward jets is presented. The study is done on parton level using RAPGAP 2.08 [11] as event generator. None of the earlier mentioned "ntuples" are used. Instead the standard HZTOOL package [23] and the routine HZ98143 [24], where a previous analysis was implemented together with all the event selection cuts, was used. The CONE jet finding algorithm was applied on the MC generated events.

The histograms, shown in fig. 7.2, give the forward jet cross-section for two different cuts in the transverse momenta of the forward jets, $p_{\perp,jet} < 3.5$ and $p_{\perp,jet} < 5.0$. Both statistical and systematic errors are included in the data. The cut $p_{\perp,jet} > 5.0$ GeV ensures a better jet selection than the cut $p_{\perp,jet} > 3.5$ GeV described in section 4.2, since the jets become harder, such that it is easier for the jet algorithm to separate and find the jets. This can be seen from the better agreement between the data and the Monte Carlo. However for the cut $p_{\perp,jet} > 5.0$ GeV the statistical error consequently becomes larger.

In the histograms of fig. 7.2 the importance of contributions from the resolved virtual photon process is illustrated. In RAPGAP, higher order parton emissions are calculated by DGLAP evolution calculations. The dashed histogram in fig. 7.2 corresponds to first order QCD matrix element calculations and higher order parton emissions generated by the DGLAP evolution. One can see that this calculation alone cannot describe the measured cross-section. However, if the resolved virtual photon is also taken into account in the calculations, the Monte Carlo cross-section is increased by almost a factor 2 and good agreement with data is obtained. In this case a DGLAP evolution is also allowed between the photon and the hard scattering vertex, as can be seen in fig. 7.1. The histograms show an increase in the cross-section for decreasing x. Due to kinematic cuts, the rise is not visible in the first bin.

This part of the work also had the purpose to get the RAPGAP steering file correctly adjusted to provide reasonable agreement with the experimental data for coming studies, for example different proton density functions were tried. For the first Monte Carlo runs the difference between the data and the Monte Carlo was large, but after changes of the proton structure function and the photon structure function good agreement was achieved. The GRV 94 HO DIS-scheme is used as the proton structure function. Also the QCD scale Λ_{QCD}

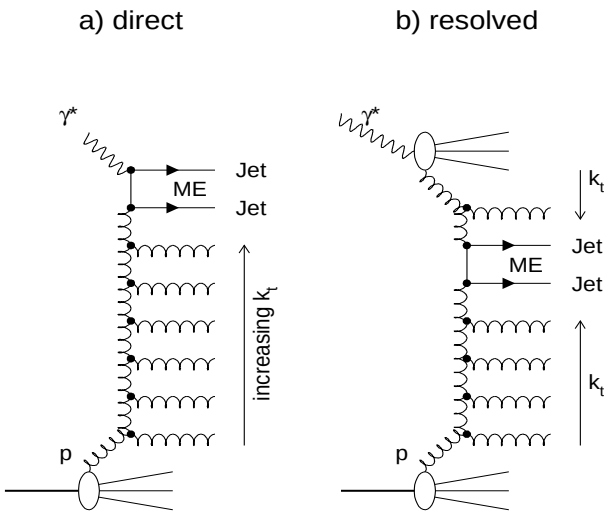

Figure 7.1: *(a) The figure shows a process where the photon is not resolved. (b) When the photon is resolved in the process a DGLAP evolution is allowed also between the photon and the hard scattering vertex. The arrows indicates the ordering in transverse momenta, k_t, which is characteristic for the DGLAP dynamics.*

is of big importance. Λ_{QCD} is a constant related to α_s and its value depends on the number of quark flavours used in the calculations. According to PDFLIB[1] $\Lambda_{QCD} = 0.200$ GeV^2 is recommended for four flavours and the proton density function used here (GRV 94 HO). Instead $\Lambda_{QCD} = 0.296$ GeV^2 is used, which corresponds to a value measured by H1, and gives a good agreement between the data and the Monte Carlo. For the resolved photon structure function the Schuler-Sjostrand [25] set is used.

I also studied the multiplicity of the forward jets. In about 1% of all events there exists more than one jet. This is a small fraction, and in future treatments in the analysis only one forward jet is considered per event.

[1]Parton Density Function Library

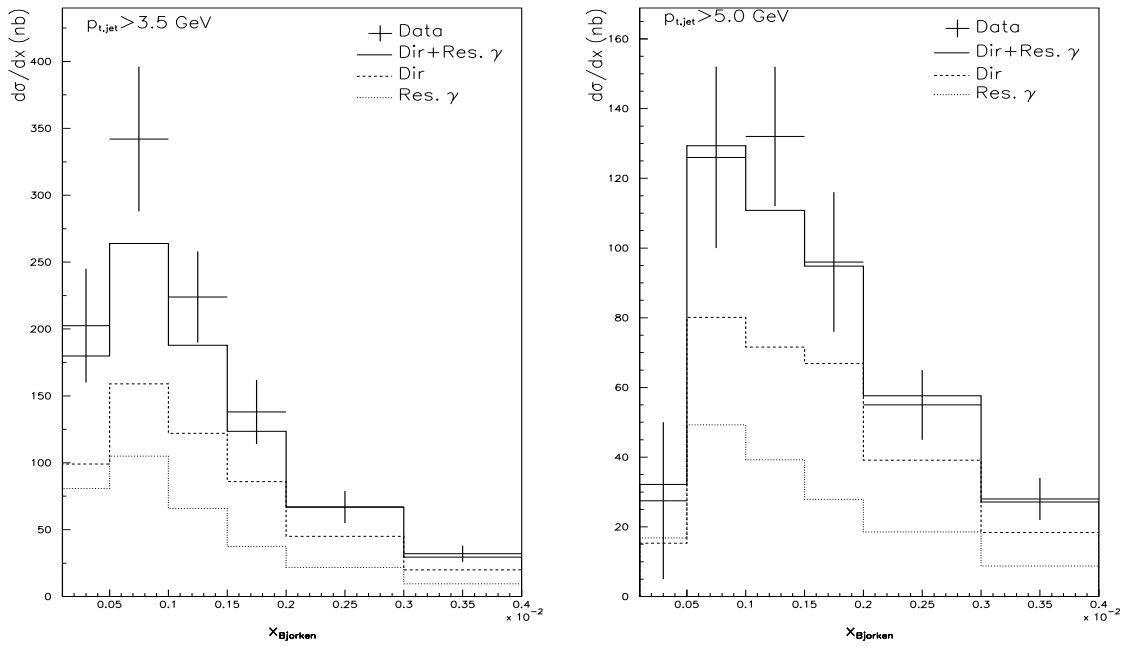

Figure 7.2: *The forward jet cross-section as a function of x in the region $0.0001 < x < 0.004$, for two different cuts in $p_{\perp,\,jet}$. Kinematic cuts make the increase in $\frac{d\sigma}{dx}$ at low x suppressed in the first bin. The direct distribution (Dir) and the resolved photon distribution (Res. γ) is shown separated and added. Both the statistical and the systematic errors are included for the data.*

Chapter 8

A Short Monte Carlo Study of Diffractive Exchanges

In RAPGAP one has the possibility to generate diffractive events using mainly 4 different exchange models; Pomerons, Reggeons, neutral pi-mesons and charged pi-mesons.

The Pomeron has already been treated in earlier chapters, and it has also been mentioned that the Pomeron and the Reggeon are sitting on two different Regge trajectories with different energy dependence on $x_{\mathbb{P}}$. Also the pi-mesons (pions) belong to a Regge trajectory. The contribution of one-pion-exchange (OPE) to the proton structure function, F_2, has been calculated. The OPE-process can be understand if the proton is assumed to be surrounded by a cloud of both charged and neutral virtual pions, and that in some cases of electron-proton scattering the exchanged photon is "hitting" one of these virtual pions outside the proton, instead of one of the partons inside the proton. Since the pions are colorless, also this gives rise to a rapidity gap event.

Here a Monte Carlo study was performed in order to investigate the contribution from various possible exchange mechanisms in diffractive scattering. The Monte Carlo simulations have been done for light quarks (u,d,s). The result is shown in fig. 8.1, where the cross-section is plotted as a function of $x_{\mathbb{P}}$, where $\mathbb{P}$ stands for any exchange. The total cross-sections for the measured region, i.e. $x_{\mathbb{P}} < 0.2$, are shown in table 8.1. The Pomeron exchange is dominating for smaller $x_{\mathbb{P}}$, whereas the contributions from $\pi^{\pm}$ and π^0 are very small in the studied region. In section 9.3, where the ratio, diffractive to inclusive forward jets, is studied, these results will come into use.

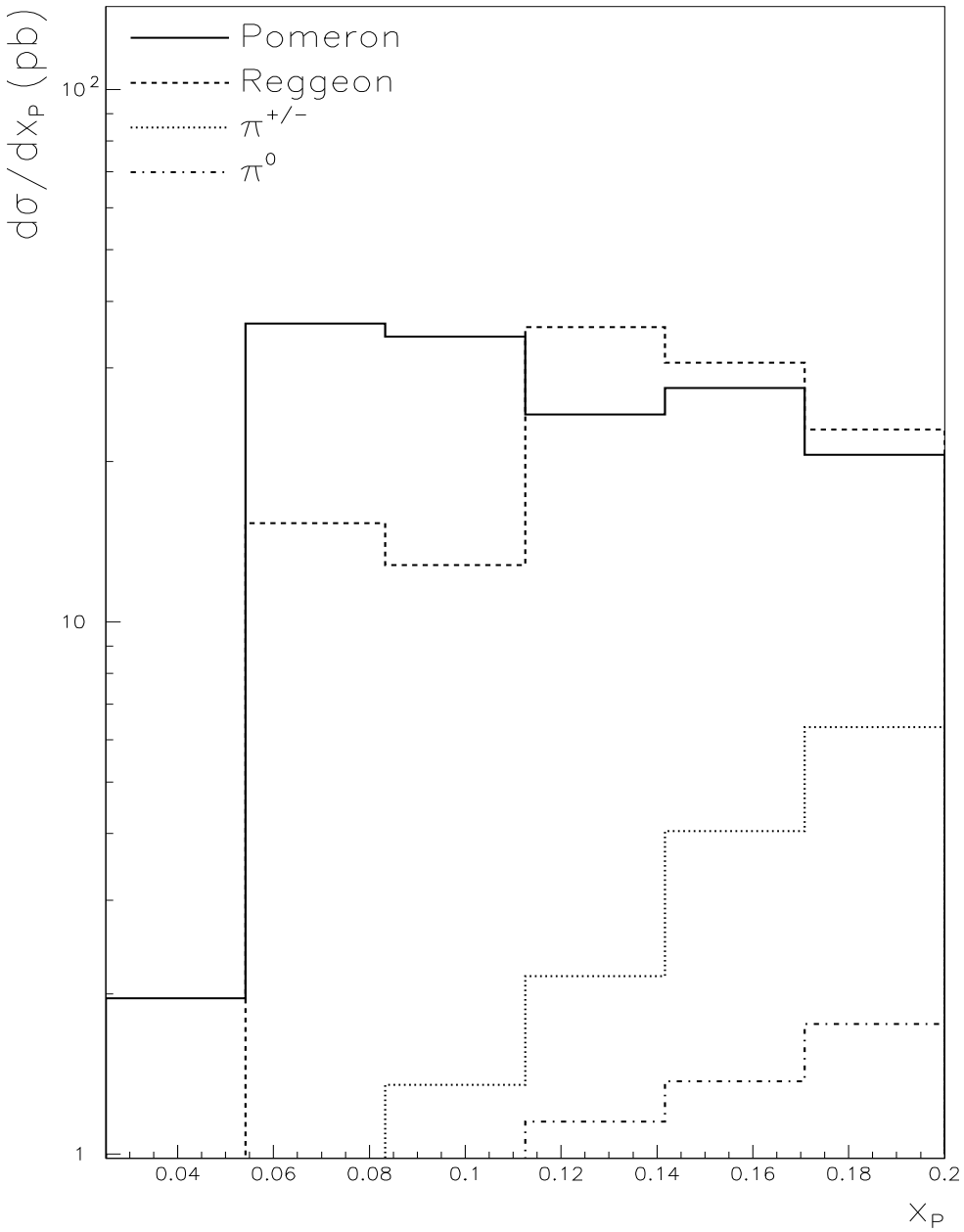

Figure 8.1: *The cross-section plotted as a function of $x_{I\!P}$ for different diffractive exchange mechanisms in forward jet events.*

Exchange	Cross-section (nb)
$\mathbb{P}$	4.2
$\mathbb{R}$	3.4
$\pi^{\pm}$	0.4
π^{0}	0.1

Table 8.1: *The cross-section for different exchange mechanisms in diffractive forward jet events below* $x_{\mathbb{P}} = 0.2$.

Chapter 9

The Fraction of Diffractive Forward Jets in DIS

The principal aim of this diploma work was to obtain the ratio of diffractive events containing forward jets to all DIS events containing forward jets, here after denoted by R, using data collected in 1997

$$R = \frac{\text{Number of diffractive events containing forward jets}}{\text{Total number of DIS events containing forward jets}} \tag{9.1}$$

Studying this ratio can help us understand the nature of diffractive scattering. The ratio will be a variable sensitive to different exchange models or Pomeron models in the BFKL phase space (enhanced due to the forward jet selection). The predictions from various models differ significantly. The hope is to understand better the details of diffraction by studying events with forward jets.

The generator files used for the analysis consist of both RAPGAP [11] files and DJANGO [10] files. The RAPGAP files contain a large fraction of diffractive events, whereas the DJANGO files contain almost no diffractive events at all, since DJANGO is a generator constructed for simulating normal DIS events. The DJANGO files are used to estimate the background to the diffractive events. That is, for the normal DIS events only the DJANGO files where used, and for the diffractive sample the RAPGAP and DJANGO were mixed together by

$$\text{DJANGO:} \quad x_{\mathbb{P}} > 0.1 \quad \text{and } M_y > 5.0 \text{ GeV} \tag{9.2}$$

$$\text{RAPGAP:} \quad x_{\mathbb{P}} < 0.1 \tag{9.3}$$

These cuts make sure that the DJANGO phase-space and the RAPGAP phase-space do not overlap, such that they cover different parts of the diffractive phase space. For non-diffractive events $x_{\mathbb{P}}$ has no physical meaning but is only used to define the event phase space.

9.1 Corrections

In order to be able to make a physical interpretation of the measurement of R it has to be detector independent, which, at a first look, it is not since we are using detectors to select the diffractive events from the data. Therefore corrections for the influence of the detector on the measurement have to be applied. One is distinguishing between results on *detector level*, *hadron level* and *parton level*. The parton level and hadron level were discussed in the theory chapter (sec. 3.3), where we mentioned that a jet algorithm takes us from parton level to hadron level. In the data the kinematics of the events is determined on detector level only, but since we would like to determine the ratio R on the hadron level, which is more fundamental from a physics point of view, we have to take the detector effects into account. This is achieved by using Monte Carlo generated events, where the kinematics of each particle in the events have been generated at hadron level followed by a detector simulation where acceptances and resolutions, etc, of the detectors are taken into account. From the simulated events one can extract the detector effects. By taking the ratio between the cross-sections, or since the inverse luminosity cancels out, the ratio between the number of events, on detector level and hadron level as a function of the relevant kinematic variables in the Monte Carlo sample, correction factors can be calculated. The correction factors are then applied on the data. For the analysis one makes 3 different selections, one from the data, i.e. detector level, one from simulated data on detector level and one from simulated data on hadron level. The cuts made in the detector selection are the same for the data and the simulations, while the cuts for the hadronic selection are made on the variables generated at hadron level. On hadron level no detector cuts are used.

We now define the correction factors κ_{DIS} and κ_{Dif}, which are used to correct the DIS selection and the diffractive selection from detector level to hadron level.

$$\kappa_{DIS} = \frac{N(\text{DIS events on hadron level})}{N(\text{DIS events on detector level})} \tag{9.4}$$

$$\kappa_{Dif} = \frac{N(\text{Diffractive DIS events on hadron level})}{N(\text{Diffractive DIS events on detector level})} \tag{9.5}$$

where N denotes the number of events. As described above, the correction factors are obtained from the simulated events. The diffractive selection on hadron level, which will be described in next section, are performed by cuts in $x_{\mathbb{P}}$, t and M_Y, while the diffractive cuts on detector level are those described in section 4.3. For the "diffrative DIS" events, the diffractive selection is applied in addition to the DIS selection (section 4.1). If the correction factors are close to 1 there is good agreement between the detector level phase space and the hadron level phase space. The smaller the correction factors are the more reliable are results from the analysis. The correction factor are different for the forward jet events and the inclusive events. From now on we will denote hadron level by "HAD", detector level by "DET", the deep inelastic selection by "DIS" and the diffractive DIS selection by "Dif".

The following ratios are calculated:

$$R^{\text{Data, DET}} = \frac{N(\text{Data, Dif, DET})}{N(\text{Data, DIS, DET})} \tag{9.6}$$

$$R^{\text{MC, DET}} = \frac{N(\text{MC, Dif, DET})}{N(\text{MC, DIS, DET})} \tag{9.7}$$

$$R^{\text{MC, HAD}} = \frac{N(\text{MC, Dif, HAD})}{N(\text{MC, DIS, HAD})} \tag{9.8}$$

where MC simply stands for Monte Carlo simulated data. We can thus define one new correction factor for the detector effects, C, instead of the correction factors (9.4) and (9.5), to be applied on the ratio (eq. (9.1)),

$$C = \frac{R^{\text{MC, HAD}}}{R^{\text{MC, DET}}} \tag{9.9}$$

such that $C = \kappa_{Dif}/\kappa_{DIS}$, and $R^{\text{Data, HAD}} = C \cdot R^{\text{Data, DET}}$.

9.2 Hadronic Diffractive Selection

For the diffractive selection in section 4.3 we only discussed cuts used to select events on detector level. On hadron level diffractive events are selected by three additional cuts, the first two made on M_Y and t. We require that

$$M_Y < 1.6 \text{ GeV} \tag{9.10}$$

and that

$$|t| < 1.0 \text{ GeV}^2 \tag{9.11}$$

M_Y and t are defined in section 3.8. However, on hadron level each event has to be scanned to find the for the largest gap in rapidity between the final state hadrons. Then one can define the X- and Y-systems and calculate M_Y, t and $x_{\mathbb{P}}$. Also for non-diffractive events $x_{\mathbb{P}}$ is calculated from the largest gap in rapidity. The two cuts (9.10) and (9.11) improve the correlation between hadron level and detector level, and therefore also results in a correction factor C closer to 1. By applying the cut on M_Y the invariant mass of the Y-system is restricted such that the Y-system only contains the proton. Events where the rapidity gap is not closest to the scattered proton in the parton ladder would then be cut away on hadron level by the cut in M_Y, which would be the case corresponding to when the diffractive selection in section 4.3 is used (i.e. the selection on detector level). The cut in $|t|$ restricts the invariant mass of the exchange object such that the proton is not scattered at too large an angle. In that way some of the diffractive events which are rejected on

detector level due to some activity from the proton remnant in the PRT, are rejected also on hadron level.

In the plots in fig. 9.1a-c $\eta_{\max}$ is plotted versus $x_{I\!P}$ on hadron level for Monte Carlo events generated by RAPGAP. In all three plots the upper limit of $x_{I\!P}$ is 0.15, due to an implicit cut in the Monte Carlo generator. We see that if the proton is loosing a larger fraction of energy, i.e. a higher $x_{I\!P}$, there will be hadronic activity in a more forward region, i.e. a larger $\eta_{\max}$, deriving from the X-system (see fig. 3.8).

Fig. 9.1a shows the $(\eta_{\max} - x_{I\!P})$-correlation for all DIS events, i.e. the forward jet selection (eq. 4.11-4.14) and the diffractive selection (eq. 9.10-9.11) are both not applied. The plot shows a strong correlation which means that $\eta_{\max}$ on detector level is related to $x_{I\!P}$ on hadron level. Therefore one can select rapidity gap events on detector level and improve the agreement between detector level phase space and hadron level phase space. For typical diffraction such a requirement would become about $x_{I\!P} < 0.04$. For the requirement of forward jets however we will see that one has to change this cut to $x_{I\!P} < 0.1$.

Fig. 9.1b shows the same $(\eta_{\max} - x_{I\!P})$-correlation, with the requirements for forward jets (eq. 4.11-4.14) applied, but without any diffractive requirements. The correlation is still visible, but a gap is visible in the $(\eta_{\max} - x_{I\!P})$-phase space. This region corresponds to the rapidity region where a jet is defined as a forward jet, compare cut (4.11). The cluster at high $\eta_{\max} - x_{I\!P}$ corresponds to forward jet events which have a hadron with higher rapidity than the forward jet.

In the same plot we also see that a there is some events containing forward jets having an $\eta_{\max}$ below the rapidity of the forward jet. It can appear as a contradiction, but as mentioned earlier the X and the Y systems of the generated events are defined by the largest gap in rapidity. Thus, it could in some cases happen that the rapidity gap not is closest to the scattered proton. Since a jet therefore can belong to the Y system and that $\eta_{\max}$ is defined from the X system, we can have a forward jet event with an $\eta_{\max}$ lower than the rapidity of the forward jet. This will not be possible on detector level since we here, by the cut in $\eta_{\max}$, require that the rapidity gap is closest to the scattered proton.

In **fig. 9.1c** the diffractive requirements (9.10) and (9.11) have been added in addition to the forward jet selection. These additional cuts remove the cluster of events with an $\eta_{\max}$ below the rapidity region of the forward jets. A closer investigation shows us that it is the cut in M_Y that removes the events at lower $\eta_{\max} - x_{I\!P}$. This confirms our suspicion that the forward jet in some cases were clustered from the Y-system which consisted of more than just the scattered proton, i.e. for events where the rapidity gap is not closest to the proton in the parton ladder. We see that the cut in M_Y fulfills its task, it removes events where the rapidity gap not is closest to the proton in the parton ladder.

We now also define the cut in $x_{I\!P}$, which is determined such that the correction factor, C, comes close to 1. This cut will, as explained above, correspond to the cut $\eta_{\max} < 3.3$ on detector level. From fig. 9.1c we see that the cut will be around $x_{I\!P} = 0.09$. The cut

$$x_{I\!P} < 0.10 \tag{9.12}$$

turns out to give the smallest correction, C, for the events used in the analysis, and this is thus the third restriction we use to select diffractive events on hadron level. This means

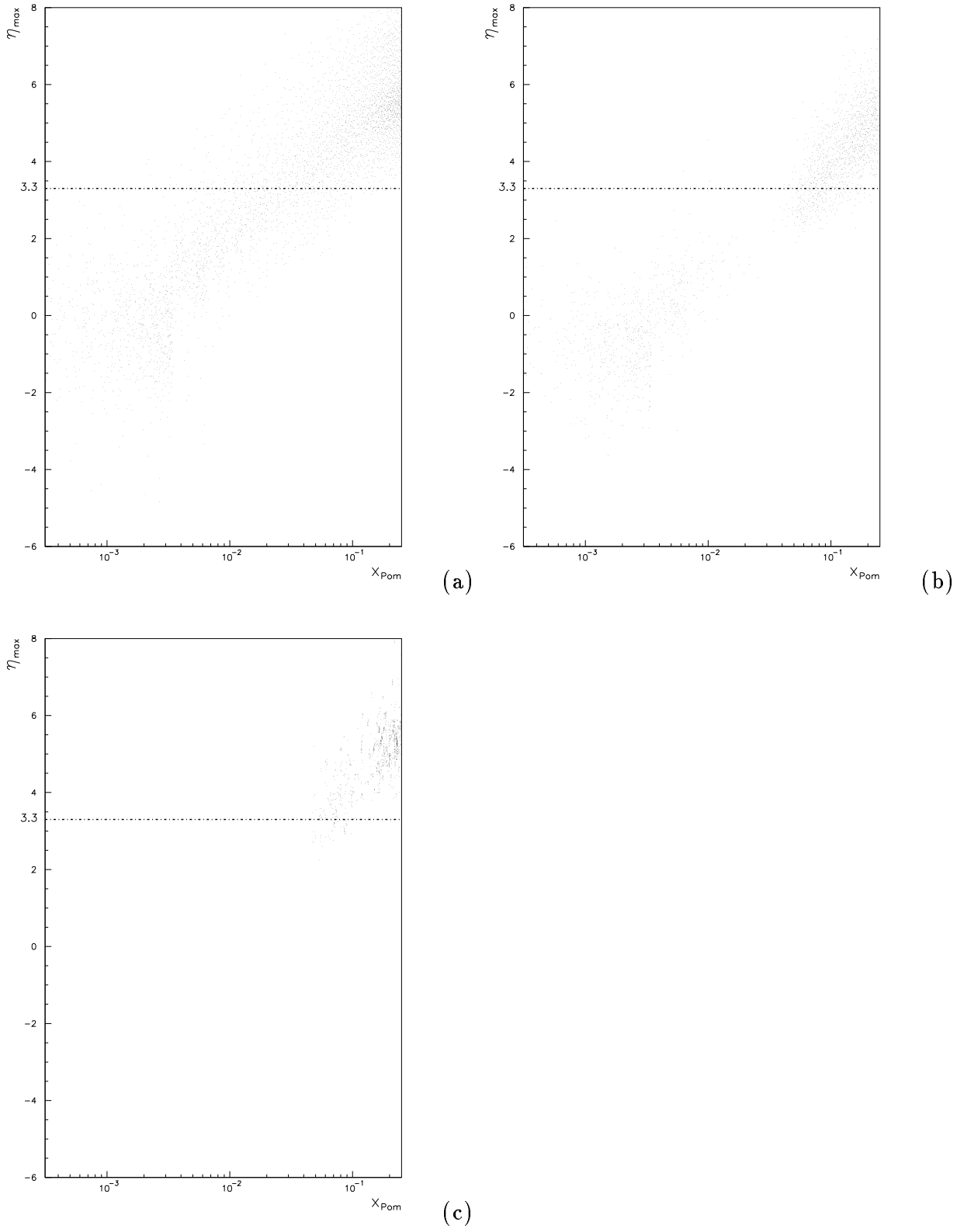

Figure 9.1: *a) $\eta_{max} - x_{I\!P}$ correlation on hadron level for all DIS events. No requirements for jets or diffraction are applied. b) The correlation when the forward jet selection (eq. 4.11-4.14) is applied, but the diffractive selection is not. c) Here the correlation is plotted for diffractive events (eq. 9.10-9.11) containing a forward jet.*

that essentially all the DJANGO generated events are cut away, which is not surprising since only diffractive events are selected by the cut in $\eta_{\max}$. $x_{\mathbb{P}} < 0.1$ is thus the cut used to select diffractive events from the forward jet selection on hadron level, corresponding the $\eta_{\max} < 3.3$ on detector level. We notice that this cut in $x_{\mathbb{P}}$ is not the same as the cut $x_{\mathbb{P}} < 0.04$, which, looking at fig. 9.1a, can be used to select diffractive events from a sample without any restrictions on the jets.

We now see that the region in phase space available for an analysis of diffractive events including a jet in the forward direction is very small and the number of events are limited. The result of the analysis is presented as a single number instead of plotting the ratio as a function of a kinematic variables, e.g. y or Q^2. A histogram would be more informative, but unfortunately the statistics is too low, such that the error per bin would be too large, and the shape of a distribution would not give us any relevant information.

9.3 The Diffractive Ratio

In the analysis we want to extract the ratio, $R = R^{\text{Data, HAD}}$, which is the number of diffractive DIS events in the data on hadron level containing a forward jet divided by the number of DIS events in the data on hadron level containing a forward jet, i.e.

$$R^{\text{Data, HAD}} = \frac{\sigma(\text{Data, Dif, HAD})}{\sigma(\text{Data, DIS, HAD})} = \frac{N(\text{Data, Dif, HAD})}{N(\text{Data, DIS, HAD})} \tag{9.13}$$

where σ denotes the forward jet cross-section and N the number of events containing forward jets. (Eq. 9.13 is equivalent to eq. 9.1.)

First the correction factors for the four different selections are calculated, and the results are shown below where κ_{DIS} is the correction factor for the normal DIS events, κ_{Dif} the correction factor for diffractive DIS events, $\kappa_{\text{DIS, forward jets}}$ the correction factor for DIS events containing forward jets and $\kappa_{\text{Dif, forward jets}}$ the correction factor for diffractive events containing forward jets. The two first corrections are not used in this analysis but indicate the influence of the detector on the data in the selected kinematical region. We see that the DIS and Dif corrections are small, being of the order of 20%.

$$\kappa_{\text{DIS}} = 1.203 \tag{9.14}$$

$$\kappa_{\text{Dif}} = 1.186 \tag{9.15}$$

$$\kappa_{\text{DIS, forward jets}} = 0.754 \tag{9.16}$$

$$\kappa_{\text{Dif, forward jets}} = 0.531 \tag{9.17}$$

The correction for the ratio, C, then becomes

$$C = 0.704 \tag{9.18}$$

9.4 Error Calculations

The statistical error of the corrected global ratio is calculated with Gauss' approximation formula, which for an arbitrary function $f(x_1 ... x_m)$ is expressed as

$$(\delta f(x_1, ...x_m))^2 = \sum_{i=1}^{m} (\delta x_i)^2 \left(\frac{\partial f}{\partial x_i}\right)^2 \tag{9.19}$$

We assume that the events used in the calculations are independent such that the error in the number of events, δN, is Poisson distributed. The error in number of events is then

$$\delta N = \pm\sqrt{N} \tag{9.20}$$

For simplicity we express the ratio as

$$R = \frac{N_1}{N_2} \cdot \frac{N_3}{N_4} \cdot \frac{N_5}{N_6} \tag{9.21}$$

where N_1, N_2, ... , N_6 are the six different samples used in the analysis, and obtain the error

$$\delta R^2 = \sum_{i=1}^{6} (\delta N_i)^2 \left(\frac{\partial R}{\partial N_i}\right)^2 \tag{9.22}$$

$$= \left(\sqrt{N_1}\right)^2 \cdot \frac{R^2}{N_1^2} + \left(\sqrt{N_2}\right)^2 \cdot \frac{R^2}{N_2^2} + ... \tag{9.23}$$

$$= R^2 \cdot \left(\frac{1}{N_1} + \frac{1}{N_2} + ...\right) \tag{9.24}$$

where i denotes the different event samples. Thus the formula for calculating the error becomes

$$\begin{aligned} \delta R^2 = R^2 \cdot \Big(& N(\text{Data}, \text{Dif}, \text{DET})^{-1} + N(\text{Data}, \text{DIS}, \text{DET})^{-1} + \\ & + N(\text{MC}, \text{Dif}, \text{DET})^{-1} + N(\text{MC}, \text{DIS}, \text{DET})^{-1} + \\ & + N(\text{MC}, \text{Dif}, \text{HAD})^{-1} + N(\text{MC}, \text{DIS}, \text{HAD})^{-1} \Big) \end{aligned} \tag{9.25}$$

9.5 Results

To obtain acceptably small corrections when converting data from detector level to hadron level, the ratio of diffractive events containing forward jets was studied for $x_{\mathbb{P}} < 0.10$. The resulting ratio on hadron level becomes

$$\boxed{R = (2.55 \pm 1.4)\%}$$

Additional Requirements	Statistics
None	$\sim 5.1 \cdot 10^6$ events
Electron candidate in SPACAL	$\sim 5.0 \cdot 10^6$ events
DIS Selection	$\sim 5.2 \cdot 10^5$ events
Forward jet selection	$\sim 7.8 \cdot 10^3$ events
Diffractive selection	54 events

Table 9.1: *Number of data events before weightings and corrections are applied.*

The number of events used to obtain the result is again seen in table 9.1. The table shows number of events before any weightings and correction factors are applied.

Looking at histogram 8.1 we see that, in the $x_{\mathbb{P}}$ region studied, the RAPGAP Monte Carlo program predicts about 50% of the diffractive events to proceed via Pomeron exchange and somewhat less than 50% via Reggeon exchange. The π-meson exchanges is close to zero in the $x_{\mathbb{P}}$ region investigated.

The ratio R for the real data above can be compared with the same ratio on hadron level for the Monte Carlo sample, eq. (9.8) with the forward jet selection applied. It was calculated to 1.2%. This is an interesting result since the prediction differs by about a factor of 2 from the measured value (but still agrees within the errors). Further Monte Carlo studies has to be done to see what kind of theoretical model that gives good agreement with the data, e.g. different Pomeron models (e.g. the resolved Pomeron model or the 2-gluon exchange model). The relevance of the resolved photon processes also has to be investigated in the future. However, due to the low statistics the error of the measured value is large, and more data would give better confidence in the measured value.

The fraction of diffractive events for the data files before the forward jet selection is applied is approximately 11%. Again we remember that a fraction of about 10% of normal diffractive events to all events is what has been measured previously at HERA.

Chapter 10

Azimuthal Asymmetry

In diffractive scattering where the proton is not fragmented, one can define the angle Φ as the azimuthal angle *between* the two scattering planes of the electron and the proton respectively. The electron plane which is spanned by the three-momenta of the incoming and the scattered electron, and the proton plane which is spanned by the three-momenta of the incoming and the scattered proton. These two planes are also referred to as the hadronic and the leptonic planes. The planes and the angle between them are shown schematically in fig. 10.1. For collisions between unpolarized electrons and protons, the diffractive cross-section as a function of Φ, $\frac{d\sigma}{d\Phi}$, can be decomposed in terms of the cross-sections of different polarization states of the exchanged photon as

$$\frac{d\sigma}{d\Phi} \sim \sigma_L + \epsilon\sigma_T - 2\sqrt{\epsilon(1+\epsilon)}\sigma_{LT}\cos\Phi + \epsilon\sigma_{TT}\cos 2\Phi \tag{10.1}$$

where σ_T and σ_L are the cross-sections for longitudinally and transversely polarized photons, σ_{LT} denotes the cross-section for interference between longitudinal and transverse polarization of the photon, whereas σ_{TT} denotes the cross-section for interference between different transverse polarizations of the photon. ϵ is a polarization parameter given by

$$\epsilon = \frac{1-y}{1-y+\frac{1}{2}y^2} \tag{10.2}$$

In the kinematic region investigated here, we have $\frac{1}{2}y^2 < 1-y$, and therefore $\epsilon \approx 1$. Neglecting σ_{TT} and rearranging the different terms in eq. (10.1) we can write the differential cross-section as

$$\frac{d\sigma}{d\Phi} \approx B(1 - A_{LT}\cdot\cos(\Phi)) \tag{10.3}$$

where A_{LT} and B are constants. B is a normalization factor including the terms independent of Φ, i.e. σ_T and σ_L. The cross-section is not symmetric. The interference between the cross-section for scattering of longitudinally and transversely polarized photons gives rise to an asymmetry in the distribution of Φ. The magnitude of the azimuthal asymmetry is determined by the asymmetry factor A_{LT}. By measuring the Φ-dependent cross-section the

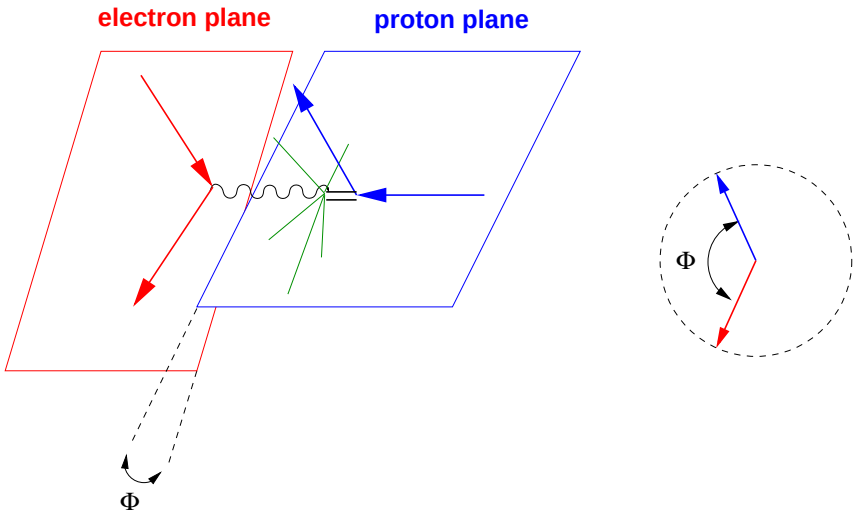

Figure 10.1: *Figure illustrating the definition of* Φ*, which is defined as the angle between the leptonic and the hadronic plane. The left and the right picture are different views of the same collision. Thus, the two* Φ*-angles are the same.*

parameter A_{LT}, which is proportional to σ_{LT}, can be determined and the interference between longitudinally and transversely polarized photons can be measured. The azimuthal asymmetry of the cross-section can be used to test models for the diffractive exchange mechanism.

10.1 The VFPS

For an accurate determination of the azimuthal angle Φ, the flight directions of both the electron and the proton have to be measured with good precision. In the case of the proton this is problematic since the proton proceeds almost unscattered in the beam-pipe where installations of detectors requires special precautions. At the moment H1 has a forward proton spectrometer (FPS), which however has a very limited acceptance and low efficiency, and it will not keep up with the upgrade of the luminosity at HERA in the year 2002. Therefore, in 2001 a "very forward proton spectrometer" (VFPS) was proposed[1], and it is suggested that this among other measurements of diffractive processes could be used for measurements of the azimuthal asymmetry. The VFPS will have larger acceptance and higher efficiency such that it will make profit of the luminosity upgrade. The VFPS will have be positioned close to the beam-pipe 220 m from the interaction vertex [26]. It will thus cover a region in the high rapidity range making it possible to detect protons scattered at small angles.

We have performed a Monte Carlo study to find out whether it would be possible to measure the azimuthal asymmetry by using the VFPS. An asymmetry in the Φ-angle was

[1]Approved in November 2001

implemented in the description of the differential cross-section in RAPGAP. This was done by modifying the calculation of four-momenta of the scattered electron and the scattered proton in the generator such that the cross-section was dependent of Φ as in eq. (10.3). The kinematic variables, i.e. the four-momentum, of the proton where then "run" through a VFPS simulator. The effect of the VFPS detector resolution was taken into account by applying smearing to the relevant kinematic variables. This means that the generated value of the kinematic variable is replaced by a Gaussian distribution of a width corresponding to detector resolution for measuring this variable. The scattered electron, detected in the SpaCal or in the LAr, is here assumed to be well measured, and no smearing of the electron kinematics is done for the calculations in this Monte Carlo analysis.

10.2 Calculating and Determining the Asymmetry

Two different methods are used here to determine the asymmetry factor, A_{LT}, one where the same function as in eq. (10.3) was fitted to the Φ-distribution, and another where a simple formula was used. The smeared asymmetry factor was compared with the asymmetry factor as implemented in RAPGAP, here referred to as the true asymmetry.

The angle Φ was calculated for each event. Also this calculation can be performed in two ways. The common geometric formula, which calculates the angle between two planes, can be used.

$$\cos\Phi = \frac{(\overline{p}_e \times \overline{p}'_e) \cdot (\overline{p}_p \times \overline{p}'_p)}{|\overline{p}_e \times \overline{p}'_e||\overline{p}_p \times \overline{p}'_p|} \tag{10.4}$$

Here the vector products of the three-momenta of the incoming electron ($\overline{p}_e$), the scattered electron ($\overline{p}'_e$), the incoming proton ($\overline{p}_p$) and the scattered proton ($\overline{p}'_p$) are used. The other method is to use the difference between the azimuthal angles, ϕ, of the electron and the proton respectively, with respect to the H1 reference system. The results two methods agreed well in both the laboratory frame and the hadronic center of mass system, i.e. the rest frame of the photon-proton system ($\gamma - p$), as can be seen in the upper pictures in fig. 10.2.

The lower plots of fig. 10.2 illustrate that the Φ-angle in the $(e-p)$-frame and the Φ-angle in the $(\gamma - p)$-frame are strongly correlated. In this Monte Carlo study all calculations were made in the laboratory frame.

The possibility to determine the asymmetry was studied for six different implemented asymmetry constants, namely $A_{LT} = \pm 0.2, \pm 0.05, \pm 0.01$. "The asymmetries", etc., in the text refers to these 6 asymmetries. Due to experimental difficulties, the asymmetry in the Φ-distribution has been poorly measured before. However, hints are given in [27], where ZEUS measured an asymmetry factor $A_{LT} = -0.049 \pm 0.058(stat.)^{+0.056}_{-0.09}(syst.)$, with errors so large that the value is consistent with zero. The ZEUS group used the Leading Proton Spectrometer (LPS), a detector equivalent to the FPS at H1, to measure Φ by the "fit method" used in section 10.3.

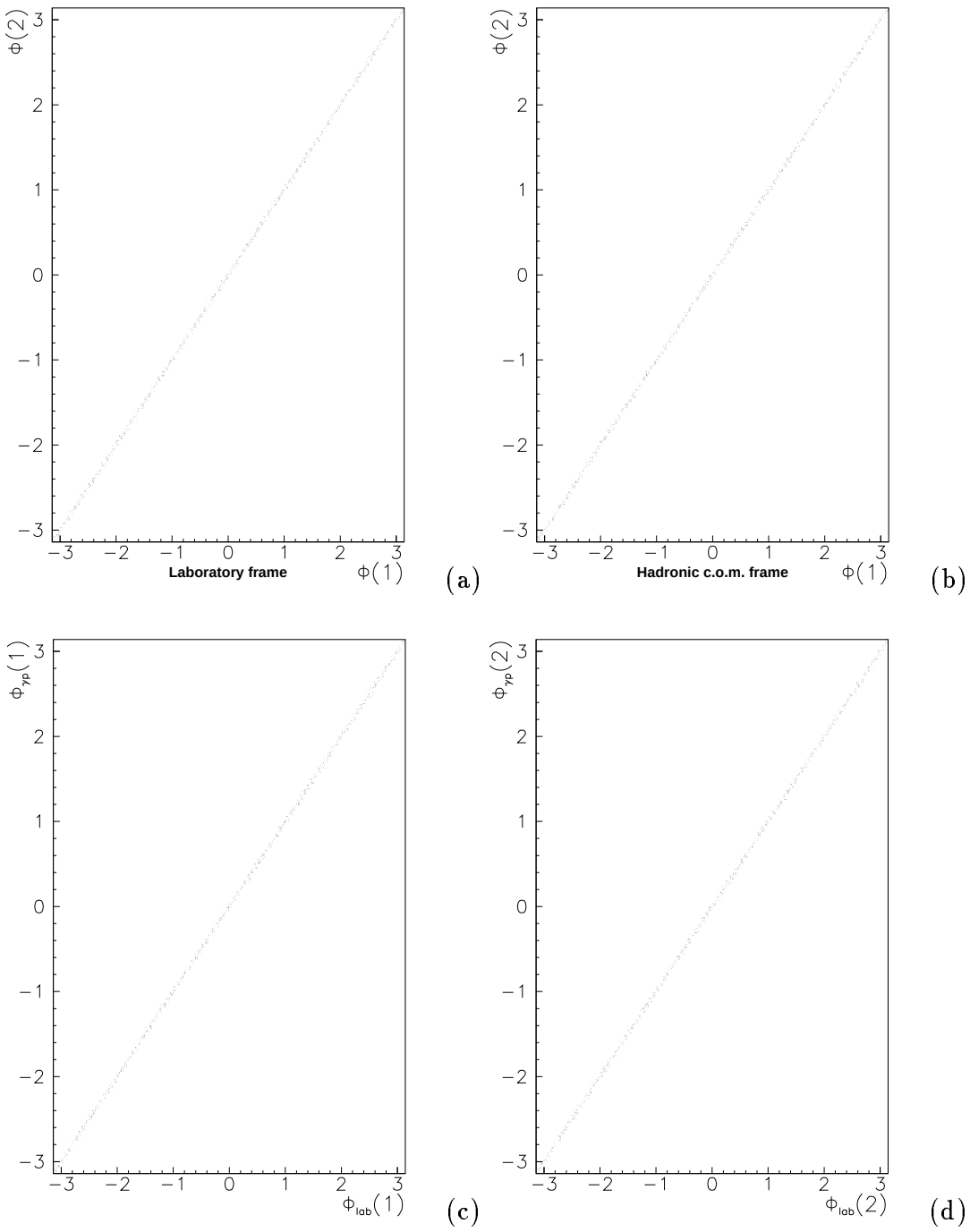

Figure 10.2: *The difference in the azimuthal angles of the scattered electron and the scattered proton, $\phi(1)$ and calculated from eq. (10.4), $\phi(2)$, gives the same result, both in the laboratory frame (a) and the hadronic center of mass system (b). The Φ-angle in the $\gamma - p$ frame and the Φ-angle in the laboratory frame are correlated, both using the difference in the azimuthal angles of the scattered electron and the scattered proton (c) and using eq. (10.4) (d). Here $A_{LT} = 0.2$ is implemented in the Monte Carlo, although the magnitude of the asymmetry is not affecting the plots.*

Analysing diffractive scattering often involves very low statistics especially when diffractive forward jets (as has been seen in this thesis) or diffractive charm production is required. It is therefore interesting to investigate what statistics is needed in order to obtain sensitivity to the asymmetry. This is one of the main purposes of this study. Up to the limit of the detector resolution higher statistics will then improve the precision of the measurement since the statistical errors become smaller, and systematical errors becomes more easily corrected.

10.3 Results

The magnitude of the asymmetry has been determined from two different methods. The first is to use the formula

$$A_{LT} = \frac{\pi}{2} \cdot \frac{\sigma(\cos(\Phi > 0)) - \sigma(\cos(\Phi < 0))}{\sigma(\cos(\Phi > 0)) + \sigma(\cos(\Phi < 0))} \tag{10.5}$$

In the second method the size of the asymmetry is extracted from a fit to the measured Φ-distribution using eq. (10.3). In this formula B is a normalization constant which does not influence the result.

The Gauss' approximation formula, eq. (9.19) gives an expression for the error δA_{LT}, which can be written

$$\delta A_{LT} = \frac{\pi}{2 \cdot \sqrt{\text{Number of events}}} \tag{10.6}$$

We see from this expression that the error is independent of the size of the asymmetry and depends on the statistics only. Using eq. (10.6) we can directly calculate what statistics is necessary for a significant measurement assuming the different magnitudes of the asymmetry. For $A_{LT} = \pm 0.01$ we then find that about 25000 events are needed in order to get a statistical error which is of the same size as the signal. For $A_{LT} = \pm 0.05$ the corresponding number is approximately 1000 events and for $A_{LT} = \pm 0.20$ it would be sufficient with less than 100 events.

The systematic error will set a limit to how small asymmetries can be measured. The size of the systematical error determines how much statistics one has to collect for a certain asymmetry size since the rule of thumb is that it does not make sense to have a statistical error much smaller than the systematic error.

The results obtained from the simulations using eq. (10.5) are shown in table 10.1 and results from the fit to the asymmetry distribution in table 10.3. In the tables 10.2 and 10.4 the results without detector simulations are shown for the two methods of determing the asymmetry. In addition the simulated Φ-distributions for three different values of A_{LT} are shown in fig. 10.3 together with the fitted curves.

The tables give values for the asymmetries using different sizes of the statistical sample. The number of events for which the proton is detected in the VFPS is given in the first

line and underneath in brackets is also the generated number of events specified, except for the tables where no detector effects are considered since here all events are accepted in the measurement. In the column on the left hand side the true values of the asymmetries are given. Reconstructed values for the asymmetries are only presented for event samples giving a statistical error of the same size or smaller than the signal, which has to measured. Systematic deviations of the measured asymmetry from the true value indicate effects coming from the simulation of the detector performance. (Comparing the measured asymmetries in tables where the VFPS simulation is used with measured values in the tables where the pure generated values are measured we see that it is the detector effects that scrambles the measurements, not the methods.)

Looking at the values presented in the tables 10.2 and 10.4 we can observe that they in essentially in all cases are consistent with the true asymmetries within the statistical errors. There are no deviations which indicate that anything should be wrong with the two methods of determing the asymmetry.

The results in the tables 10.1 and 10.3 give a hint that it might be difficult to measure an asymmetry as low as ± 0.01 due to the influence of the detector. However it might be that the fit method is less sensitive to detector effects than what is the case using the formula (10.5) to calculate the asymmetry.

Also for the higher asymmetry values we observe that the fit method gives a better reconstruction of the asymmetries than calculations from eq. (10.5), which in general gives systematically too small values. The only exeption is for $A_{LT} = 0.05$ where the values agree with the true asymmetry at high enough statistics.

With the available material it is difficult to explain the observed deviations and a better understanding would require more detailed investigations of detector effects. That would for example involve studies of different detector parts. Considering the errors the two methods agree, except for the cases where $A_{LT} = -0.01$ and eq. (10.5) was used to determine the asymmetry (table 10.1).

In the case of the fit method different bin widths were used to extract the values. The general conclusion is that with increasing statistics more bins give a better measurement of the asymmetry. However, there is no big difference in the measured values for the different number of bins used. In some cases 3 bins are insufficient for making a good fit. This can clearly be seen for the asymmetries ± 0.20 in table 10.4 where no detector effects are considered. Here a fit with 6 and 10 bins gives values closer to the true asymmetry than a fit with 3 bins only.

10.4 Summary

The possibility of measuring azimuthal asymmetries in electron-proton diffractive scattering using a Very Forward Proton Spectrometer has been studied. Different assumptions for the magnitude of asymmetry has been implemented into the Monte Carlo generator RAPGAP in order to investigate what statistical sample is needed for a significant determination of the asymmetry considering the acceptance and resolution of the detector. By

comparing the number of generated events with the number of accepted events one conclude that the acceptance of the VFPS is around 22%, which is an improvement compared to the old FPS.

This analysis can be regarded as a pre-investigation, in order to find out whether it will be possible to measure azimuthal asymmetries by using the VFPS. A more complete analysis would involve e.g. more Monte Carlo simulations and also studies of larger amount of different asymmetries such that histograms could be plotted. We have shown that the Φ-asymmetry can be measured by using two different methods (table 10.2 and 10.4), but the detector effects has to be more carefully investigated and understood in order to increase the confidence in the measurements.

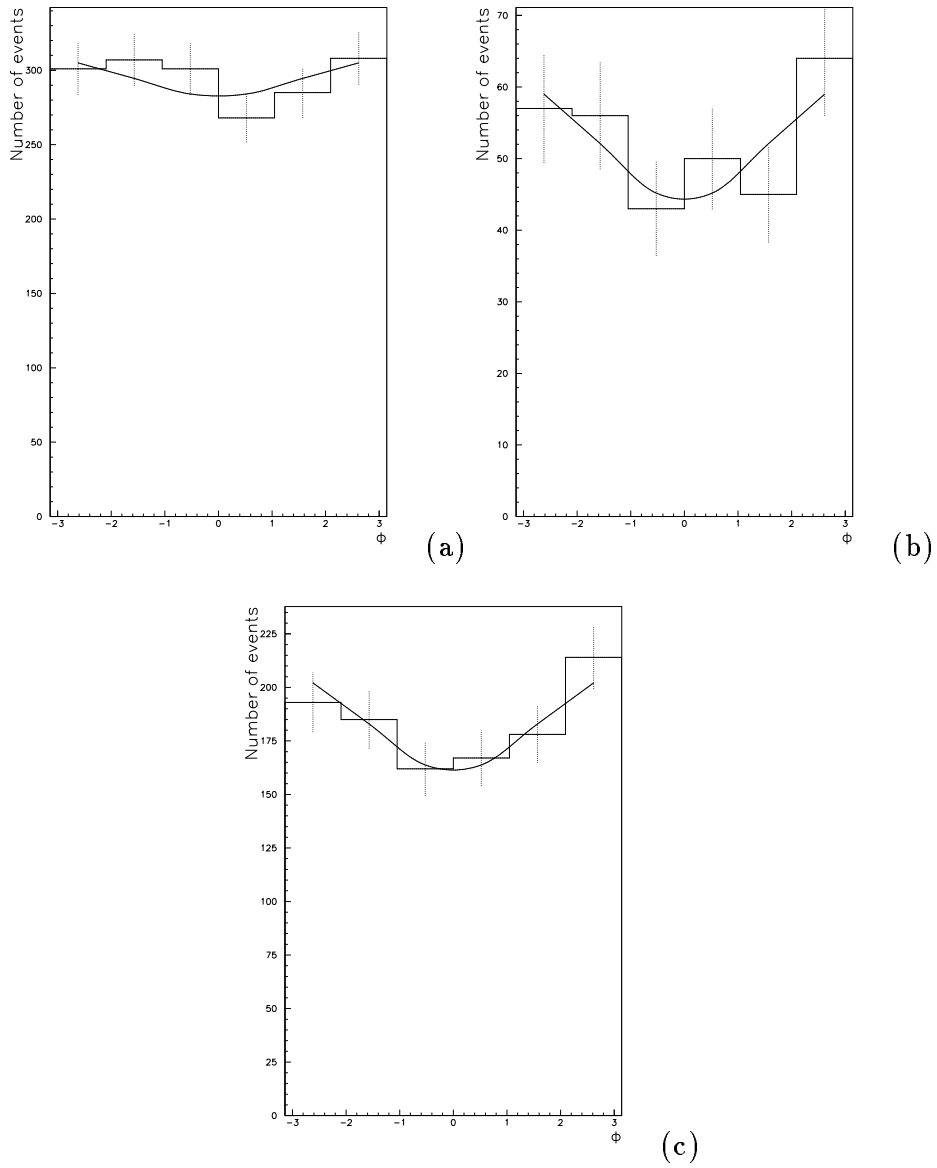

Figure 10.3: Φ-*distributions for (a) 1750 events,* $A_{LT,true} = -0.05$, $A_{LT,fit} = -0.04 \pm 0.03$*; (b) 330 events,* $A_{LT,true} = -0.05$, $A_{LT,fit} = -0.15 \pm 0.08$ *and (c) 1100 events,* $A_{LT,true} = -0.2$, $A_{LT,fit} = -0.11 \pm 0.08$*. The function* $B(1 - A_{LT} \cdot cos(\Phi))$ *is here fitted to the* Φ-*distributions.*

True Asymmetry factor	Calculated Asymmetry Number of events					
	∼330 (1500)	∼1100 (5000)	∼1750 (8000)	∼2230 (10000)	∼11000 (50000)	∼25000 (114000)
0.01	-	-	-	-	-	0.021
0.05	-	0.131	0.111	0.097	0.051	0.057
0.20	0.200	0.200	0.141	0.137	0.131	0.131
-0.01	-	-	-	-	-	0.011
-0.05	-	0.009	-0.014	-0.013	-0.030	-0.021
-0.20	-0.133	-0.168	-0.147	-0.133	-0.134	-0.127
Error: ±	∼0.09	∼0.05	∼0.04	∼0.02	∼0.014	∼0.009

Table 10.1: *The table shows calculated azimuthal asymmetries for different simulated asymmetry factors, A_{LT}, and number of events. In the right columns are the calculated asymmetry factors shown. The number inside the parentheses shows the number of generated events.*

True Asymmetry factor	Calculated Asymmetry without Detector Effects Number of events					
	330 -	1100 -	1750 -	2200 -	11000 -	25000 -
0.01	-	-	-	-	-	0.016
0.05	-	0.066	0.023	0.037	0.045	0.052
0.20	0.143	0.203	0.197	0.203	0.215	0.207
-0.01	-	-	-	-	-	-0.034
-0.05	-	-0.019	-0.074	-0.690	-0.048	-0.048
-0.20	-0.152	-0.174	-0.208	-0.206	-0.194	-0.198
Error: ±	∼0.09	∼0.05	∼0.04	∼0.02	∼0.014	∼0.009

Table 10.2: *Azimuthal asymmetries for different simulated asymmetry factors, A_{LT}, not smeared in the detector simulation and number of events. In the right columns are the calculated asymmetry factors shown.*

True asymm-etry factor	Nr. of bins	Fitted Asymmetry					
		Number of events					
		∼330 (1500)	∼1100 (5000)	∼1750 (8000)	∼2200 (10000)	∼11000 (50000)	25000 (11400)
0.01	3	-	-	-	-	-	0.013
	6	-	-	-	-	-	0.022
	10	-	-	-	-	-	0.022
0.05	3	-	0.109	0.100	0.080	0.048	0.051
	6	-	0.119	0.115	0.086	0.057	0.053
	10	-	0.101	0.094	0.069	0.054	0.054
0.20	3	0.169	0.164	0.127	0.122	0.104	0.116
	6	0.141	0.151	0.125	0.133	0.131	0.133
	10	0.138	0.145	0.129	0.126	0.136	0.137
-0.01	3	-	-	-	-	-	-0.011
	6	-	-	-	-	-	-0.005
	10	-	-	-	-	-	-0.005
-0.05	3	-	0.021	-0.009	0.016	-0.004	-0.072
	6	-	0.020	-0.012	0.006	-0.009	-0.011
	10	-	0.021	-0.175	-0.010	-0.013	-0.018
-0.20	3	-0.072	-0.135	-0.113	-0.117	-0.113	-0.110
	6	-0.097	-0.168	-0.129	-0.126	-0.136	-0.131
	10	-0.130	-0.176	-0.140	-0.128	-0.135	-0.134
Error: (±)		∼0.08	∼0.04	∼0.03	∼0.03	∼0.014	∼0.009

Table 10.3: *Azimuthal asymmetries, calculated from a fit made to the* Φ*-distribution, for different simulated azimuthal asymmetries,* A_{LT}*, number of bins and number of events. The fitted asymmetry factors are shown in the right columns. The number inside the parentheses shows the number of generated events.*

True asymm-etry factor	Nr. of bins	Fitted Asymmetry without Detector Effects					
		Number of events					
		330	1100	1750	2200	11000	25000
		-	-	-	-	-	-
0.01	3	-	-	-	-	-	-0.002
	6	-	-	-	-	-	0.006
	10	-	-	-	-	-	0.004
0.05	3	-	0.012	0.091	0.097	0.042	0.050
	6	-	0.010	0.085	0.086	0.043	0.051
	10	-	0.073	0.071	0.068	0.044	0.052
0.20	3	0.219	0.214	0.181	0.167	0.173	0.171
	6	0.227	0.226	0.205	0.193	0.194	0.200
	10	0.210	0.221	0.203	0.194	0.200	0.207
-0.01	3	-	-	-	-	-	-0.008
	6	-	-	-	-	-	-0.011
	10	-	-	-	-	-	-0.010
-0.05	3	-	-0.095	-0.075	-0.055	-0.047	-0.041
	6	-	-0.082	-0.091	-0.056	-0.054	-0.049
	10	-	-0.075	-0.059	-0.051	-0.051	-0.051
-0.20	3	-0.364	-0.236	-0.169	-0.177	-0.163	-0.175
	6	-0.383	-0.259	-0.193	-0.206	-0.190	-0.201
	10	-0.322	-0.244	-0.189	-0.204	-0.193	-0.211
Error: ($\pm$)		$\sim$0.08	$\sim$0.04	$\sim$0.03	$\sim$0.03	$\sim$0.014	$\sim$0.009

Table 10.4: *Azimuthal asymmetries, calculated from a fit made to the Φ-distribution, for different simulated azimuthal asymmetries, A_{LT}, number of bins and number of events. The fitted asymmetry factors are shown in the right columns. Here is no detector effects considered.*

Chapter 11

Summary and Conclusions

The practical work of the thesis started with a short Monte Carlo study of forward jet production in DIS. It was shown that the inclusion of resolved photon events increses the forward jet cross-section by about a factor of 2, which is necessary to describe the data.

The fraction of diffractive forward jet events in DIS was measured to be about 2.6%, a ratio that is 3-6 times smaller than the fraction of normal diffractive DIS events. This result derives from two similar analysis, where different Monte Carlo files were used. The second analysis was performed to improve the corrections from detector level to hadron level, which was successfully done.

The ratio of events with a forward jet in diffractio was measured in the region of about $x_{\mathbb{P}} < 0.10$. A region where the correction for detector effects was small. By Monte Carlo studies it was also shown that in this region the experimental data could be described if it was assumed that about 50% of the exchange is due to Reggeons and about 50% is due to Pomerons. In the end the ratio can help us understand the structure of the Pomeron or e.g. the relevance of the 2 gluon exchange model and the resolved Pomeron model.

The possibilities of studying azimuthal asymmetries by using the VFPS simulator were investigated, and it turned out that effects of asymmetries larger than or equal to $A_{LT} = \pm 0.05$ can be seen with a statistical sample of about 1000 events, whereas for smaller asymmetries one needs a larger event sample in order to decrease the errors in the calculations. Two methods were used to determine the asymmetry, and both gave similar results.

Chapter 12

Acknowledgement

I would like to thank the people at the Particle Physics department in Lund University. Leif Jönsson and Hannes Jung for supervision. Leif, especially for help with the writing. Hannes, especially for his never ending stream of ideas and suggestions. Martin Karlsson for always helping and patiently answering questions. Mattias Davidsson for feedback on the presentation of the work. Frank-Peter Schilling (DESY, University of Heidelberg) for some help on the diffraction.

Bibliography

[1] B.R.Martin and G.Shaw, Particle Physics, 1992, ISBN 0-521-66226-5.

[2] I. Abt et al., *Nucl. Instrum. Meth.* **A386** (1997) 348.

[3] D. Green, The Physics of Particle Detectors, 2000, ISBN 0-471-97252-5.

[4] P. Thompson, Open Charm Production in Inclusive and Diffractive DIS at HERA, 1999, PhD thesis.

[5] F.-P. Schilling, Diffractive Jet Production in Deep-Inelastic e^+p Collisions at HERA, 2001, PhD thesis.

[6] P. Sievers, Untersuchungen zur Verbesserung der Energiemessung im Ruckwartsbereich des H1-experiment, 1999, dip. thesis.

[7] Brown, Selected papers of Richard Feynman, page 487, 2000, iSBN 981-02-4131-3.

[8] B. Andersson, The Lund Model, 1998, iSBN 0 521 42094 6.

[9] T. Sjostrand, L. Lonnblad, S. Mrenna, (2001) .

[10] L. Lonnblad, , in *Hamburg 1991, Proceedings, Physics at HERA, vol. 3* 1440-1445. (see HIGH ENERGY PHYSICS INDEX 30 (1992) No. 12988).

[11] H. Jung, *Comp. Phys. Commun.* **86** (1995) 147.

[12] G. Ingelman, A. Edin, J. Rathsman, *Comput. Phys. Commun.* **101** (1997) 108.

[13] G. Marchesini et al., *Comput. Phys. Commun.* **67** (1992) 465.

[14] V. Gribov, L. Lipatov, *Sov. J. Nucl. Phys.* **15** (1972) 438 and 675.

[15] L. Lipatov, *Sov. J. Nucl. Phys.* **20** (1975) 94.

[16] G. Altarelli, G. Parisi, *Nucl. Phys.* **B 126** (1977) 298.

[17] Y. Dokshitzer, *Sov. Phys. JETP* **46** (1977) 641.

[18] V. Fadin, E. Kuraev, L. Lipatov, *Sov. Phys. JETP* **45** (1972) 199.

[19] Y. Balitsky, L. Lipatov, *Sov. J. Nucl. Phys.* **28** (1978) 822.

[20] H. Jung, L. Jonsson, H. Kuster, *Eur. Phys. J.* **C 9** (1999) 383.

[21] J.R. Forshaw and D.A. Ross, Quantum Chromodynamics and the Pomeron, 1997, ISBN 0-521-56880-3.

[22] M. Karlsson, Jet Reconstruction and its Application in Studies of Parton Dynamics, 2001, lic. thesis.

[23] J. Bromley et al., , prepared for Workshop on Future Physics at HERA (Preceded by meetings 25-26 Sep 1995 and 7-9 Feb 1996 at DESY), Hamburg, Germany, 30-31 May 1996.

[24] C. Adloff et al., *Nucl. Phys.* **B538** (1999) 3.

[25] G. A. Schuler, T. Sjostrand, *Phys. Lett.* **B376** (1996) 193.

[26] L. Favart et al., *H1-5/00-582, PRC-01/00* (2000).

[27] ZEUS Collaboration, Results on inclusive diffraction with the ZEUS LPS at HERA, International conference on HEP, Budapest, July, 2001.

[28] M. Davisson, Jet Production and Parton Dynamics in Deep Inelastic Scattering, 2001, PhD thesis.

[29] M. Kuhlen, QCD at HERA, The Hadronic Final State in Deep Inelastic Scattering, 1999, ISBN 3-540-65118-7.

[30] G. Wolf, Deep inelastic scattering at large energy and momentum transfers: Recent results from HERA collider, 2001.

[31] C. Adloff et al., *Eur. Phys. J.* **C20** (2001) 29.

[32] C. Adloff et al., *Eur. Phys. J.* **C6** (1999) 421.

The references [28, 29, 30, 31] and [32] are not directly refered to in the text but have been relevant for my studies.